Acta Biomaterialia 186 (2024) 470–488

Contents lists available at ScienceDirect

Acta Biomaterialia

journal homepage: www.elsevier.com/locate/actbio

Full length article

Bioinspired oriented calcium phosphate nanocrystal arrays with bactericidal and osteogenic properties

Lorenzo Degli Esposti[a], Damiano Squitieri[b], Camilla Fusacchia[a,c], Giada Bassi[a,d], Riccardo Torelli[e], Davide Altamura[f], Erika Manicone[f,g], Silvia Panseri[a], Alessio Adamiano[a], Cinzia Giannini[f], Monica Montesi[a], Francesca Bugli[b,e,*], Michele Iafisco[a,*]

[a] Institute of Science, Technology and Sustainability for Ceramics (ISSMC), National Research Council (CNR), Via Granarolo 64, 48018 Faenza, Italy
[b] Dipartimento di Scienze Biotecnologiche di Base, Cliniche Intensivologiche e Perioperatorie, Università Cattolica del Sacro Cuore, 00168 Rome, Italy
[c] Dipartimento di Scienze Chimiche, della Vita e della Sostenibilità Ambientale, Università di Parma, Via delle Scienze 11/A, 43124, Parma (PR), Italy
[d] Department of Neuroscience, Imaging and Clinical Science. University of G. d'Annunzio, Via dei Vestini 31, 66100, Chieti, Italy
[e] Dipartimento di Scienze di Laboratorio e Infettivologiche, Fondazione Policlinico Universitario A. Gemelli IRCCS, 00168 Rome, Italy
[f] Istituto di Cristallografia, Consiglio Nazionale delle Ricerche (CNR), Via Amendola 122/O, 70126 Bari, Italy
[g] Dipartimento di Chimica, Università degli studi di Bari Aldo Moro, Via Orabona 4, 70126 Bari, Italy

ARTICLE INFO

Article history:
Received 12 April 2024
Revised 22 July 2024
Accepted 1 August 2024
Available online 6 August 2024

Keywords:
Antibacterial nanostructured surface
Antibiotic resistance
Calcium phosphate
Bio-inspired material
Osteogenic differentiation

ABSTRACT

The global diffusion of antibiotic resistance poses a severe threat to public health. Addressing antibiotic-resistant infections requires innovative approaches, such as antibacterial nanostructured surfaces (ANSs). These surfaces, featuring ordered arrays of nanostructures, exhibit the ability to kill bacteria upon contact. However, most currently developed ANSs utilize bioinert materials, lacking bioactivity crucial for promoting tissue regeneration, particularly in the context of bone infections. This study introduces ANSs composed of bioactive calcium phosphate nanocrystals. Two distinct ANSs were created through a biomineralization-inspired growth of amorphous calcium phosphate (ACP) precursors. The ANSs demonstrated efficient antibacterial properties against both Gram-negative (*P. aeruginosa*) and Gram-positive (*S. aureus*) antibiotic resistant bacteria, with up to 75 % mortality in adhered bacteria after only 4 h of contact. Notably, the ANS featuring thinner and less oriented nano-needles exhibited superior efficacy attributed to simultaneous membrane rupturing and oxidative stress induction. Moreover, the ANSs facilitate the proliferation of mammalian cells, enhancing adhesion, spreading, and reducing oxidative stress. The ANSs displayed also significant bioactivity towards human mesenchymal stem cells, promoting colonization and inducing osteogenic differentiation. Specifically, the ANS with thicker and more ordered nano-needles demonstrated heightened effects. In conclusion, ANSs introduced in this work have the potential to serve as foundation for developing bone graft materials capable of eradicate site infections while concurrently stimulating bone regeneration.

Statement of significance

Nanostructured surfaces with antibacterial properties through a mechano-bactericidal mechanism have shown significant potential in fighting antibiotic resistance. However, these surfaces have not been fabricated with bioactive materials necessary for developing devices that are both antibacterial and able to stimulate tissue regeneration. This study demonstrates the feasibility of creating nanostructured surfaces of ordered calcium phosphate nano-needles through a biomineralization-inspired growth. These surfaces exhibit dual functionality, serving as effective bactericidal agents against Gram-negative and Gram-positive antibiotic-resistant bacteria while also promoting the proliferation of mammalian cells and inducing osteogenic differentiation of human mesenchymal stem cells. Consequently, this approach holds promise in the context of bone infections, introducing innovative nanostructured surfaces that could be utilized in the development of antimicrobial and osteogenic grafts.

* Corresponding authors.
E-mail addresses: francesca.bugli@unicatt.it (F. Bugli), michele.iafisco@issmc.cnr.it (M. Iafisco).

https://doi.org/10.1016/j.actbio.2024.08.001
1742-7061/

1. Introduction

According to the World Health Organization (WHO), antimicrobial resistance is one of the top 10 global public health threats facing humanity. The diffusion of drug-resistant pathogens increases the risk of disease spread, severe illness, and death [1]. Antibiotic-resistant bacterial strains are usually treated with massive doses of broad-spectrum antibiotics, but this approach has a low efficacy and poses the risk of inducing the emergence of new multi- and pan-resistant bacteria, also known as "superbugs", which are not treatable with any existing antimicrobial drug [2].

This urgently calls for novel alternatives to fight infections. In this regard, there is high interest on antibacterial nanostructured surfaces (ANSs). This term refers to materials that possess micro- or nanostructured surfaces with the ability to inhibit bacterial adhesion (antifouling effect) or to kill bacteria (bactericidal effect) [3]. ANSs were inspired by biological structures; for example certain insect wings as those of some cicada species are endowed with antibacterial and antifungal properties [4]. In detail, they are covered by ordered arrays of nano-pillars with height of less than 1 μm and diameter of less than 100 nm, which can kill bacteria by rupturing or exerting an excessive mechanical stretching on the bacterial cell wall - a multi-layered structure protecting the microbe [4,5].

The development of biocide-free surfaces for killing bacteria could potentially offer an advantage against antibiotic resistance, as this physical bactericidal mechanism is nonspecific. Unlike antibiotic drugs, which disrupt specific bacterial metabolic pathways and can be rapidly counteracted via mutations and horizontal gene transfer [6], the a-specific nature of this physical mechanism may mitigate resistance development. Additionally, ANSs were also proved to be non-cytotoxic toward eukaryotic cells, as these cells exhibit resilience to the deformational stress due to their larger dimensions and more elastic membrane compared to bacteria [7].

ANSs were generated on various materials using several top-down methods including lithography, casting, etching, etc. The resulting structures take the form of ordered arrays of nano-pillars, nano-needles, nano-cones, nano-spikes, nano-wires, nano-pores, etc. [8]. Despite achieving significant milestones, this research has a key gap: ANSs were primarily produced using materials that are biocompatible but inert, lacking bioactivity. These materials include silicon, diamond, metals (e.g. titanium and its alloys, gold, etc.) and some polymers (PMMA, PEEK, etc.) [8,9]. This issue underscores the need for the development of materials that are antimicrobial upon contact while also being cell-instructive and bioactive. For example, in the case of bone infection, the therapeutic approach requires not only eradicating the infection, but also simultaneously regenerating the destroyed bone, typically using osteo-inductive graft materials. Therefore, biomaterials-based bone grafts for the regeneration of infected osseous tissue should locally impede bacterial growth while providing favorable host reparative cells that stimulate immunomodulatory, angiogenic and osteogenic events.

In this regard, the aim of this work is to generate ANSs made of biocompatible, bioactive, and osteo-inductive synthetic calcium phosphate (CaP) materials. CaPs are considered among the best materials for developing bone graft substitutes due to their chemical similarity to the bone mineral, which leads to high biocompatibility and bioactivity that promotes bone formation [10]. Typically CaP materials have been rendered antimicrobial through functionalization with antibiotics such as drugs, silver and other ions, and quaternary ammonium salts [11]. However, a critical limitation of these strategies is their transience, as the leaching of the antimicrobials is subject to depletion over time. The decreasing antibiotic concentration leads to a progressively weaker antibacterial effect, which, at the same time, may also promote antimicrobial resistance [12,13].

Another advantage of CaPs for the development of ANSs is that they can be finely shaped by biomineralization-inspired approaches. Biomineralization is defined as the forming process of inorganic minerals by living organisms. Through evolution, nature has established robust pathways and mechanisms to produce precisely controlled biominerals distinct from minerals found in non-biological systems. These pathways involve the presence of soluble additives such as crystallization modifiers, inhibitors, or nucleation agents [14]. The accumulating knowledge on biomineralization has attracted the attention of materials scientists as a source of inspiration to achieve advanced CaP materials with complex shape, hierarchical organization and well-defined size, morphology, and structure [14]. For example, previous works have shown that is possible to grow ordered CaP nano-needles hierarchically-organized in precise arrays [15-17]. In brief, it was found that in presence of an aqueous solution of calcium, phosphate, and fluoride ions the surface of an amorphous calcium phosphate (ACP) substrate first partially dissolves and then recrystallizes into oriented arrays of fluorapatite (FA, $Ca_{10}(PO_4)_6F_2$) nanocrystals [15-17].

Currently, the number of CaP-based ANSs reported in literature is scarce [18-20]. In these limited studies, hydroxyapatite (HA, $Ca_{10}(PO_4)_6(OH)_2$) nano-pillars were grown using bottom-up approaches either onto titanium surfaces by electrophoretic deposition or onto CaP substrates by hydrolysis and reprecipitation of a CaP precursor. In all cases, a significant antibacterial effect against Gram-negative bacteria was observed [18-20]. Similarly to other ANSs, it was found for CaPs that the antibacterial effect depended on the nano-topographical features (nanocrystals height, spacing, diameter, etc.) [18]. However, the structure-effect correlation is still unclear, and many questions remain unanswered. Moreover, there are no reports on the efficacy of CaP-based ANSs against Gram-positive bacteria. This type of bacteria are known to be more resistant to physical bactericidal effect due to their thicker peptidoglycan layer attached to teichoic and lipoteichoic acids in the cytoplasmic membrane, compared to the thinner outer membrane of Gram-negative bacteria, which possesses porins and lipopolysaccharides [13]. Additionally, there is no information on the interaction of CaP-based ANSs with eukaryotic cells. Therefore, the development of ANSs using CaP materials is an exciting new field that requires further investigations.

In this work we have generated two ANSs based on organized CaP nano-needles arrays, differing in terms of nano-topography, by using a bottom-up approach inspired by biomineralization processes. We assessed the morphology, chemical and structural composition of ANS through X-ray diffraction in theta/2theta geometry and electron microscopy as well as by X-ray scattering techniques in transmission (scanning SAXS/WAXS) and grazing incidence (GI-WAXS/GISAXS) reflection geometry. The antimicrobial activity of these ANSs was evaluated against clinically relevant antibiotic-resistant bacterial strains. Specifically, an extensively drug-resistant *P. aeruginosa* strain isolated from a respiratory sample was chosen as Gram-negative bacteria model, while Methicillin-resistant *S. aureus* strain isolated from a positive blood culture was used as Gram-positive representative. Bacteria adhesion onto ANSs, microbial viability and morphology were studied to correlate antibacterial activity of the samples with their nanostructure. Furthermore, we preliminarily assessed the *in vitro* biocompatibility of the ANSs towards VERO epithelial cells, a mammalian cell line commonly used to evaluate cytotoxicity. This assessment involved studying cell viability, adhesion, and morphology. The induction of oxidative stress in bacterial and mammalian cells by ANSs was also evaluated. Finally, we examined the influence of the CaP-based ANSs on human Adipose-derived Mesenchymal Stem Cells (Ad-MSCs), a well-known *in vitro* model suitable for testing the osteogenic differentiation and regenerative potential of bone tissue [21,22]. This assessment included analyzing cell viability and proliferation, cell

adhesion and morphology, and the potential ability of samples to trigger the osteogenic differentiation pathway.

2. Materials and methods

2.1. Reagents

Acetic acid ($C_2H_4O_2$, ≥99.0 % pure), calcium chloride dihydrate ($CaCl_2{\cdot}2H_2O$, ≥99,0 % pure), dexamethasone (water soluble, BioReagent, suitable for cell culture), ethanol absolute anhydrous (CH_3CH_2OH, 99,9 % pure), β-glycerophosphate disodium salt hydrate (BioUltra, ≥99.0 %), hydrochloric acid (HCl, ≥37,0 % pure), glutaraldehyde solution (grade II, 25 % in H_2O, $OHC(CH_2)_3CHO$) magnesium ascorbyl phosphate ($C_6H_6Mg_{1.5}O_9P{\cdot}xH_2O$, powder form, white, ≥95 % pure), paraformaldehyde (PFA, $HO(CH_2O)_nH$, reagent grade, crystalline), monobasic potassium phosphate (KH_2PO_4, ≥98,0 % pure), dibasic potassium phosphate (K_2HPO_4, ≥98,0 % pure), 2-propanol (C_3H_8O, ≥99,5 % pure), sodium acetate ($C_2H_3O_2Na$, referred as CH_3COONa, ≥99.0 % pure), sodium cacodylate trihydrate ($(CH_3)_2AsO_2Na{\cdot}3H_2O$, ≥98,0 % pure), sodium carbonate monohydrate ($Na_2CO_3{\cdot}H_2O$, 99.5 % pure), sodium citrate tribasic dihydrate ($Na_3(C_6H_5O_7){\cdot}2H_2O$, referred as Na_3Cit, ≥99,0 % pure), sodium chloride (NaCl, ≥98 % pure), sodium deoxycholate ($C_{24}H_{39}NaO_4$, ≥97 % pure), sodium dodecyl sulphate ($CH_3(CH_2)_{11}OSO_3Na$, ≥99 % pure) sodium fluoride (NaF, ≥99,0 % pure), disodium p-nitrophenyl phosphate (pNP-PO_4, ≥97 % pure), sodium phosphate dibasic (Na_2HPO_4, ≥99,0 % pure), TritonX-100 (2-[4-(2,4,4-trimethylpentan-2-yl)phenoxy]ethan-1-ol), Tris–HCl (≥99 % pure), and Trypan Blue powder (BioReagent, suitable for cell culture) were supplied by Sigma-Aldrich (St. Louis, MO, USA). Fetal Bovine Serum (FBS), Minimum Essential Medium supplemented with l-Glutamine (MEM), Minimum Essential Medium α GlutaMAX with l-Glutamine (α-MEM GlutaMAX), 1 % Penicillin/Streptomycin solution (pen/strep, 100 U/mL-100 µg/mL), recombinant human basic-Fibroblast Growth Factor (hbFGF), Trypsine- EDTA 0.5 % no phenol red (10X) and Phosphate Buffer Saline (PBS) were supplied by Gibco (Life technologies - Thermo Fisher scientific, Waltham, Massachusetts, USA). Presto Blue Cell viability reagent, LIVE/DEAD Viability/Cytotoxicity kit (for mammalian cells), Actin-Red 555 ReadyProbes reagent (rhodamine phalloidin), 4′,6-diamidino-2-phenylindole dihydrochloride (DAPI) and Tri Reagent solution were supplied by Invitrogen (Life technologies - Thermo Fisher scientific, Waltham, Massachusetts, USA). The High-Capacity cDNA Reverse Transcription Kit and the TaqMan Gene Expression Assay Kits were purchased from Applied Biosystems (Life technologies - Thermo Fisher scientific, Waltham, Massachusetts, USA). Saline solution (0,9 wt.% sodium chloride) was purchased from bioMérieux (Marcy-l'Étoile, France). Trypsin-EDTA 10x and Normal Goat Serum (NGS) was supplied from Euroclone (AddLife AB, Stockholm, Sweden). Bovine Serum Albumin Low Endotoxin (BSA) was purchased from PAA – The Cell Culture Company (Headquarter Austria, 4061 Pasching). The Direct-zol RNA MiniPrep purification kit was purchased from Zymo Research (Irvine, 17062 Murphy Ave, United States). All the solutions were prepared with ultrapure water (18.2 MΩ·cm, 25 °C, Arium pro, Sartorius).

2.2. ACPs synthesis

Two different ACPs were prepared, one without stabilizer (ACP) and the other stabilized by citrate (Cit-ACP). ACP was synthesized according to the procedure reported by Carella et al. [15]. Equal volumes of two solutions composed of (A) 20 mM $CaCl_2$ and (B) 20 mM Na_2HPO_4 were mixed at 4 °C under vigorous stirring. The precipitate was immediately collected by centrifugation (12,500 rpm, 2 min, 0 °C) and washed twice - first with ultrapure water at 4 °C and then with absolute ethanol at 4 °C. The product was freeze-dried and stored at −20 °C.

Cit-ACP was synthesized as reported in [23] by vigorous stirring at room temperature equal volumes of two solutions composed of (A) 100 mM $CaCl_2$ + 400 mM Na_3Cit and (B) 120 mM Na_2HPO_4 + 200 mM Na_2CO_3. Before mixing, the pH of solution (B) was adjusted to 9.5 with HCl. After 60 s of stirring, the formed precipitate was collected by centrifugation (7000 rpm, 5 min, 4 °C) and repeatedly washed with ultrapure water. Subsequently, it was freeze-dried overnight and stored at 4 °C until use.

2.3. Substrate disks preparation

Cit-ACP and ACP powders were compression-molded to form disk substrates. For each molding, 150 mg of Cit-ACP or ACP powders were placed in a cylindrical steel mold with an inner diameter of Ø 12 mm and hydraulic pressure was applied at levels of 37, 137, or 800 MPa for 10 min. After molding, disks with a thickness of 1 mm were obtained. The substrates were stored at 4 °C until use.

2.4. Growth of ANSs

To grow oriented arrays of nanocrystals on the surface of ACP and Cit-ACP substrates, a growth solution (GS) was prepared following the methods reported by Onuma et al. and Carella et al. [15,16] with some modifications. The composition of the GS is reported in Supplementary Table 1. It was prepared by adding the following solutions to 31.5 mL of ultrapure water: (A) 3.5 mL of 40 mM K_2HPO_4 + 40 mM KH_2PO_4 + 1 M CH_3COONa, (B) 140 µL of 1 M $CaCl_2$, and (C) 350 µL of 52.6 mM NaF. Before mixing, the pH of solution A was adjusted to 6.3 with 1 M acetic acid. The solutions were added in the specific order and left to stir for 2 min between each addition.

Each substrate was placed in a Petri dish, immersed in 35 mL of GS, and subjected to static incubation at 37 °C for 24 h. The codes of the prepared samples are detailed in Table 1. Samples obtained from ACP and Cit-ACP substrates pressed at 137 MPa were named ACP GS and Cit-ACP GS, respectively. Control samples were prepared by incubating the substrates pressed at 137 MPa in 35 mL of ultrapure water at 37 °C for 24 h (ACP H_2O and Cit-ACP H_2O). After incubation, whether in GS or water, the substrates were removed from the solution, washed first with water and then with pure ethanol, and left to dry at room temperature.

2.5. Materials characterization

Field emission-gun scanning electron microscopy (FEG-SEM) analyses of the samples were conducted using a ΣIGMA FEG-SEM microscope (ZEISS NTS Gmbh, Oberkochen, Germany). The samples were cut into pieces with a surgical blade and fixed to aluminum SEM stubs using graphitic glue, positioning the surface upward for observing nanocrystals morphology from a top view. For micrographs of arrays in section, fractured substrate pieces were mounted sideways. All samples were sputter-coated with gold using an E5100 Sputter Coater (Polaron Equipment, Watford, Hertfordshire, UK) to enhance electrical conductance. FEG-SEM micrographs were captured in secondary electrons mode at an acceleration voltage of 4 kV. For each sample at least four randomly selected fields were acquired at magnifications ranging from 5000× to 50,000×. Nanocrystals morphology was analyzed with software ImageJ [24].

X-ray diffraction (XRD) patterns of the samples were recorded on a D8 Advance diffractometer (Bruker, Karlsruhe, Germany) using Cu Kα radiation ($\lambda = 1.54178$ Å) generated at 40 kV and 40 mA in

Table 1
Code of the samples and preparation conditions. The selected samples tested with bacteria and eukaryotic cells are reported in italics.

Sample	Mineral phase	Substrate compression condition	Growth condition
ACP 37 MPa GS	ACP	37 MPa	GS solution
ACP 137 MPa GS (ACP GS)	ACP	137 MPa	GS solution
ACP 800 MPa GS	ACP	800 MPa	GS solution
Cit-ACP 37 MPa GS	Cit-ACP	37 MPa	GS solution
Cit-ACP 137 MPa GS (Cit-ACP GS)	Cit-ACP	137 MPa	GS solution
Cit-ACP 800 MPa GS	Cit-ACP	800 MPa	GS solution
ACP H_2O	ACP	137 MPa	Water
Cit-ACP H_2O	Cit-ACP	137 MPa	Water

theta/2theta geometry. XRD patterns were recorded from 10 to 80° 2θ with a step size of 0.02° and a counting time of 1 s.

(GI)SAXS/(GI)WAXS measurements were performed at the XMI-Lab [25], equipped with a Fr-E+ Superbright X-ray micro-source (Rigaku, Tokyo, Japan) coupled to a SMAX3000 SAXS/WAXS camera via a focusing optics and a three-pinhole beam shaping system delivering a 0.2 mm (diameter) beam spot at sample position. A Fuji Image Plate served as detector, placed downstream the sample at 87 mm for GIWAXS or 28 mm for WAXS, and read off-line by a Raxia scanner. SAXS data were collected in scanning mode by a Triton multiwire gas-filled detector placed at about 2 m distance downstream the sample. The transmitted (unscattered) X-ray intensity was collected simultaneously at each sample position by a pin-diode located inside the beamstop, to obtain absorption contrast microscopies and transmission coefficients for SAXS intensity normalization. The average WAXS pattern over the scanned sample area was also collected simultaneously to the SAXS data, thanks to a hole in the middle of the Image Plate letting the small-angle-scattered beam pass through. Scanning SAXS data were composed in microscopies by using the in-house developed program SUNBIM [26]. SAXS and WAXS data were calibrated by using Ag Behenate (deposited as a thin film) or Si (from NIST, deposited on a glass substrate) powder standards, respectively, and in the case of WAXS data a flat detector correction was applied as implemented in SUNBIM, without any baseline interpolation. A high-precision goniometer with piezoelectric motors was used for sample alignment in GI-WAXS measurements: the incidence angle was set to 0.2°, 1° or 2° for all measurements to check depth-dependence of the diffraction signal. Samples were kept at about 0.1 mbar vacuum pressure during measurements. GIWAXS and WAXS data were fitted by using the program FullProf [27].

Transmission electron microscopy (TEM) in bright field mode and selected area electron diffraction (SAED) mode were used to observe morphology, size, and crystallinity of individual nanocrystals in a dry state. Micrographs were acquired with a Tecnai F20 microscope (Fei Corp., Hillsboro, OR, USA) equipped with a Schottky emitter and operating at 200 KeV. The overgrown layers of nanocrystals were scraped from the substrates and dispersed in isopropanol by sonication. A droplet of the finely dispersed suspension was then allowed to evaporate under room temperature and atmospheric pressure on a holey film supported on a copper grid. Single crystal spot SAED patterns were indexed with the software ProcessDiffraction [28].

Citrate release from Cit-ACP substrates with different compression-molding pressures was determined by UV–VIS spectroscopy. Cit-ACP substrates were incubated in ultrapure water at 37 °C for 8 h. Afterwards, a 700 µL aliquot of the medium was collected and acidified with 100 µL of HCl 1 M to shift citrate dissociation towards the non-deprotonated form as reported in literature [29]. The resulting solution was measured with a Lambda 750 spectrophotometer (Perkin-Elmer, Waltham, MA, USA) in the range 200–300 nm. Citrate signal was revealed as an absorption shoulder at 210 nm and quantified through a calibration curve of standard Na_3Cit solutions.

2.6. ANSs antimicrobial activity evaluation

2.6.1. Bacterial strains

The antimicrobial efficacy of ANSs compared to flat surfaces was assessed using clinically relevant bacterial strains. An extensively drug-resistant (XDR) Gram-negative *Pseudomonas aeruginosa* strain was isolated from a respiratory specimen, exhibiting resistance against Meropenem, Ertapenem, and Imipenem. Additionally, a Methicillin-resistant Gram-positive *Staphylococcus aureus* strain was obtained from a positive blood culture. Antibiotic susceptibility testing followed the EUCAST 2023 clinical breakpoints (The European Committee on Antimicrobial Susceptibility Testing- Clinical breakpoints - bacteria (v 13.1). Both strains were cultured on 5 % sheep blood Tryptic Soy Agar (bioMérieux, Marcy-l'Étoile, France).

2.6.2. Bacteria viability evaluation

Confocal imaging was conducted to assess cytocidal effect of ANSs against bacteria. Bacteria inocula equal to 1 McFarland standard turbidity (approximately 3×10^8 CFU/mL) in saline solution were prepared with Densicheck plus (bioMérieux, Marcy-l'Étoile, France). One milliliter of each inoculum was then brought into contact with tested surfaces in a 24-wells plate (Corning, New York, USA), which was incubated at 37 °C, 5 % CO_2 for 4 h in New Brunswick Excella E24 Series (New Brunswick scientific; Edison, New Jersey, USA). To perform the differential staining between live and dead bacterial cells the LIVE/DEAD BacLight bacterial viability kit (Thermo Fisher scientific, Waltham, Massachusetts, USA) was used according to manufacturer's instructions. Fluorescent staining visualization was carried out with Eclipse Ti-E Nikon confocal microcopy (Nikon Europe B.V, Amstelveen, The Netherlands). The excitation wavelengths used were 469 nm and 586 nm while emission wavelengths used were at 525 nm and 647 nm for green and red channels, respectively. Quantitative analysis of fluorescence emission was performed with ImageJ Fiji Software (Version 1.53 c) [30].

2.7. ANSs biocompatibility evaluation

2.7.1. Mammalian cell line

Biocompatibility studies on ANSs were conducted using the renal epithelial cell line of VERO E6 monkey (ATCC No CRL-1586). The cells were cultured and amplified in 25 cm^2 rectangular canted neck cell culture flask (Corning, New York, USA) with MEM adjusted to contain 10 % FBS and 1 % Penicillin/Streptomycin solution.

2.7.2. Mammalian cells viability evaluation

VERO cells at 90 % of confluence, assessed with bright field microscopy, were completely detached with Trypsin-EDTA 1x obtained by dilution in PBS through a 3-minute incubation at 37 °C and 5 % CO_2 in Steri-cult CO_2 incubator (Thermo Fisher scientific, Waltham, Massachusetts, USA). To neutralize trypsin action 5 mL of FBS were added. Subsequently, the cells were transferred to 50 mL conical tube (Corning, New York, USA) and centrifugated at 1000 rpm for 10 min with Consul 21R centrifuge (Or-

toalresa, Madrid, Spain). The obtained pellets were then resuspended and counted with NucleoCounter® NC-200™ (Chemometec, Allerød, Denmark). Approximately 10^6 cells/mL were seeded onto the tested surfaces in a 24-wells plate and incubated for 24 h at 37 °C and 5 % CO_2. Subsequently, the LIVE/DEAD viability/cytotoxicity kit for mammalian cells (Thermo Fisher scientific, Waltham, Massachusetts, USA) was used according to manufacturer's instructions. Fluorescent staining visualization was analyzed with Cytation5 multimode reader (Biotek, Winooski, Vermont, USA). The excitation wavelengths used were 469 nm and 586 nm, while emission wavelengths were at 525 nm and 647 nm for green and red channels, respectively. Quantitative analysis of fluorescence emission was conducted with ImageJ Fiji Software (Version 1.53 c).

2.8. Cell morphology evaluation

Bacteria inocula and VERO cells were prepared and incubated on ANSs and control surfaces as reported above. Subsequently, both types of samples were dehydrated through immersion in crescent gradient of ethanol concentration, from 30 to 100 %, with a multi-step procedure lasting 10 min each. The samples were then metallized with gold using a High-Resolution Sputter Coater AGB7234 (Agar Scientific, Stansted, UK). The morphology of cells on surfaces at low magnification were observed with a Supra 25 SEM microscope (Zeiss, Oberkochen, Germany). Representative micrographs were acquired in secondary electrons mode at an acceleration voltage of 15 kV. For each sample at least four randomly selected fields were acquired at magnification of 15,000×. High-magnification SEM micrographs of cells were observed with a ΣIGMA FEG-SEM microscope (Zeiss, Oberkochen, Germany), in this case representative micrographs were acquired in secondary electrons mode at an acceleration voltage of 4 kV at magnification up to 150,000×. For ease of visualization, cells in SEM micrographs were colorized with the software GIMP as micrograph post-processing.

2.9. Quantification of reactive oxygen species induced by ANSs

The induction of oxidative stress by nanostructured surfaces towards bacterial and mammalian cells was evaluated using the DCFDA/H2DCFDA cellular ROS assay kit (Abcam, Cambridge, United Kingdom). *P. aeruginosa* and *S. aureus* cells (around 3×10^8 CFU/mL) in saline solution were placed in contact with tested and control surfaces in a 24-well plate for 4 h. VERO cells at a concentration ranging from 1.2×10^6 cells/mL to 4×10^6 cells/mL were grown in DMEM + 10 % FBS in contact to ACP and Cit-ACP surfaces (along with their respective controls). Subsequently, bacterial and mammalian cells were collected by centrifugation, and the DCFDA staining was performed according to manufacturer's instructions. Fluorescent quantification was conducted in a 96-wells black plate optimized for fluorescence contexts (Nunc, Roskilde, Denmark) using a Cytation5 multimode reader (Biotek, Winooski, Vermont, USA). The fluorescent readings were performed with excitation / emission wavelength at 485 nm / 535 nm.

2.10. Cytocompatibility and differentiation of Human Adipose-Derived Mesenchymal Stem Cells evaluation

2.10.1. Cell culture

Human Primary Adipose-Derived Mesenchymal Stem Cells (Ad-MSCs) purchased from American Type Culture Collection (ATCC PCS-500–011) were cultured in α-MEM GlutaMAX with 15 % FBS, 10 ng/mL, hb-FGF and 1 % of pen/strep, hereafter referred to as standard media. Cells were detached from the culture flask by trypsinization, centrifuged, and the cell number and viability were determined by Trypan Blue Dye Exclusion test. All cell-handling procedures were performed under sterile laminar flow hood and cell cultures were incubated at 37 °C with 5 % CO_2 under controlled humidity conditions.

2.10.2. Sterilization and cell seeding on ANSs

The ANSs were sterilized twice in absolute ethanol for 10 min followed by 20 min UV irradiation in MilliQ water. Before cell seeding, the ANSs were pre-conditioned in standard media over the weekend at 37 °C before the cell seeding. Ad-MSCs were seeded at a density of 30.000 cells/sample by dripping 100 µL of cell suspension on the upper surface of ANSs, followed by 20-minute incubation at 37 °C to allow cellular pre-adhesion before the addition of the osteogenic media. The osteogenic media used was α-MEM GlutaMAX with 10 % FBS, 1 % of Pen/Strep, 10 mM β-Glycerophosphate disodium salt hydrate, 50 µg/mL Magnesium Ascorbyl Phosphate and 100 nM Dexamethasone. The samples were then incubated at 37 °C with 5 % CO_2 under controlled humidity conditions for 14 days. All cell-handling procedures were performed under sterile laminar flow hood.

2.10.3. Cell proliferation and viability evaluation

The proliferation and viability of Ad-MSCs was quantitatively analysed by Presto Blue Cell viability reagent after 1, 2, 3, 7, 10 and 14 days of culture, following the manufacturer's instructions. At each time point, the ANSs were incubated with 10 % (v/v) Presto Blue Reagent for 2 h at 37 °C in a 5 % CO_2 atmosphere under controlled humidity conditions. The reading was performed by using Fluoroskan Microplate Fluorometer (Thermo Fisher Scientific, Waltham, Massachusetts, USA) at excitation and emission wavelength of 544 and 590 nm, respectively. Three replicates were performed at each time point ($N = 3$).

A qualitative evaluation of the cell viability of Ad-MSCs was conducted using the LIVE/DEAD Assay at day 1 of culture, following the manufacturer's instructions. Briefly, the cells were washed with PBS1X and incubated with 1.3 µM of Calcein-AM to stain live cells in green and 4 µM of Ethidium homodimer-1 to stain dead cells in red for 15 min at 37 °C. Images were acquired using an Inverted Ti-E Fluorescent Microscope (Nikon, Tokyo, Japan). One biological replicate was analysed for each group ($N = 1$).

2.10.4. Cell morphology evaluation

The morphology of Ad-MSCs on the ANSs was assessed at day 3 and 14 of culture by fluorescent microscopy with Actin/DAPI staining and FEG-SEM microscopy. For the fluorescence analysis, following the manufacturer's instructions, the cells were fixed in 4 % PFA for 10 min, permeabilized in 0.1 % (v/v) Triton X-100 in PBS1X for 5 min and then incubated in the dark with Actin-Red 555 ReadyProbes reagent for 30 min. The cell nuclei were counterstained with DAPI (600 nM) reagent for 7 min in the dark. The samples were imaged by using the Inverted Ti-E Fluorescent Microscope. For the FEG-SEM analysis, the cells were washed in 0.1 M (w/v) Sodium Cacodylate Buffer (pH 7.4) and fixed in 2.5 % (v/v) Glutaraldehyde solution in 0.1 M Sodium Cacodylate Buffer for 2 h at 4 °C. The cells were dehydrated in an increasing scale of alcohol (from 30 to 100 %), mounted on aluminium stubs, and dried under hood. For the analysis, the samples were sputter-coated with 20 nm film of gold and the images were acquired under high vacuum conditions by using ΣIGMA FEG-SEM microscope (ZEISS NTS Gmbh, Oberkochen, Germany) at an acceleration voltage of 4 kV. ANSs not seeded with cells were analysed as *blank*. One biological replicate was analysed at each time point for both types of analysis ($N = 1$). For ease of visualization, cells in SEM micrographs were colorized with the software GIMP as micrograph post-processing.

2.10.5. Cellular adhesion evaluation

The cell adhesion to the ANSs was evaluated at day 3 of culture by fluorescent immunolocalization of specific markers, following the manufacturer's instructions. Briefly, the cells were fixed in 4 % PFA and blocked for nonspecific binding sites in 20 % NGS in PBS 1X for 15-minute incubation. Then, the cells were permeabilized in 0.1 % Triton X-100 in PBS 1X for 5 min and incubated overnight at 4 °C in humidity chamber with primary antibodies for Focal Adhesion Kinase (FAK, Novus Biologicals, Rabbit, 1:100) and Paxillin (Novus Biologicals, Rabbit, 1:100) in 1 % BSA in PBS 1X. The Goat Anti-Rabbit IgG Alexa 546 (Molecular Probes, Thermo Fisher Scientific, Waltham, Massachusetts, USA) was used as a secondary antibody in 1 % BSA in PBS1X solution for 1-hour incubation at room temperature in the dark. The cell nuclei were counterstained with DAPI for 7 min incubation in the dark. Images were acquired at the Inverted Ti-E Fluorescent Microscope. For each primary antibody, one biological replicate for each group was analysed ($N = 1$).

2.10.6. Gene expression

The gene expression profile of Ad-MSCs at 7 and 14 days of culture was analysed in terms of osteogenic potential. At each time point, total RNA extraction and purification were performed by Tri Reagent and Direct-zol RNA MiniPrep purification kit, following the manufacturer's instructions. The RNA quantification and purity were evaluated using the NanoDrop One Microvolume UV–Vis Spectrophotometer (Thermo Fisher Scientific, Waltham, Massachusetts, USA). The single strand cDNA was produced by performing the High-Capacity cDNA Reverse Transcription Kit (Applied Biosystems, Thermo Fisher Scientific, Waltham, Massachusetts, USA) starting from 500 ng of purified RNA. Real-Time PCR was performed on cDNA by TaqMan Gene Expression Assay Kits (Applied Biosystems, Thermo Fisher Scientific, Waltham, Massachusetts, USA) to determine the relative quantification of the target genes' expression: Bone Morphogenetic Protein 2 (BMP-2) (Hs00154192_m1), Runt-related transcription factor 2 (RUNX-2) (Hs00231692_m1) and Alkaline Phosphatase (ALP) (Hs01029144_m1). Glyceraldehyde-3-Phosphate Dehydrogenase (GAPDH) (Hs99999905_m1) was used as the housekeeping gene. Two biological samples for each condition ($N = 2$) were analysed via three technical replicates. Data were collected from QuantStudio 1 Real-Time PCR System (Applied Biosystem, Thermo Fisher Scientific, Waltham, Massachusetts, USA) and the Comparative Threshold (CT) method ($\Delta\Delta$CT) was performed to determine the relative quantification of target genes, where relative gene expression level equals to $2^{-\Delta\Delta CT}$ [31].

2.10.7. ALP activity

To evaluate the potential ability of ANSs in differentiating Ad-MSCs toward the osteogenic lineage, ALP activity was measured using an enzymatic assay based on the hydrolysis of p-nitrophenyl phosphate (pNP-PO_4) to p-nitrophenol (pNO) [32]. Briefly, the samples were washed in PBS1X and incubated twice in RIPA buffer (radioimmunoprecipitation buffer: 150 mM sodium chloride, 1.0 wt.% Triton X-100, 0.5 wt.% sodium deoxycholate, 0.1 wt.% sodium dodecyl sulphate, 50 mM Tris–HCl, pH 7.4) supplemented with protease inhibitors for 15 min on ice, using a cell scraper to lyse the cells on the material' surface. The cells lysates were collected, sonicated for 5 min at 120 Watt and 28 Hertz, and centrifuged at 4500 x g for 15 min at 4 °C to remove debris. The supernatants were combined to increase the extraction yields, obtaining a total of 200 µL of cell lysate per sample with two replicates for each group ($N = 2$). For the enzymatic assay, 25 µL of cell lysate was added to pNP-PO4 solution (10 mM solution in carbonate buffer) and allowed to react at 37 °C. The absorbance was red after 24 h of incubation at $\lambda = 405$ nm, using a Multiskan FC spectrophotometer (Thermo Fisher Scientific, Waltham, Massachusetts, USA). ALP activity was calculated by referencing a standard curve of nanomoles of p-nitrophenol, normalized to total cell number measured by Presto Blue Cell Viability Reagent, and expressed as picomoles of p-nitrophenol liberated per cell.

2.11. Statistical methods

All experiments on bacteria and VERO cells were repeated at least in triplicate to ensure reproducibility. Statistical significance between the three groups in ROS quantification was assessed with One-way analysis of variance, while LIVE/DEAD fluorescence quantification was analyzed with Two-way analysis of variance [33]. Significant difference was defined as p-value < 0.05. For Presto Blue Cell Viability Reagent, the RFU data were subtracted from the blank and presented in the graph as normalization respect to day 1 $\pm$ standard error of the mean. The gene expression data of Ad-MSCs were reported in the graphs as fold-change $2^{-\Delta\Delta CT}$ with respect to cells only as control group. For the enzymatic assay, ALP activity was reported in the graphs as picomoles/cell $\pm$ standard error of the mean. The three sets of data were analysed by Two-way analysis of Variance and Tukey's multiple comparison test. All statistical analyses were performed using GraphPad Prism software (8.0.1 version).

3. Results and discussion

3.1. Development of CaP-based ANSs

CaP-based ANSs were prepared using a biomineralization-inspired bottom-up approach. We previously demonstrated that is possible to obtain an array of oriented nanocrystals by immersing an ACP substrate in a growth solution (GS) containing calcium, phosphate, and fluoride ions [15,16]. All the three ions are necessary to achieve the organized nanostructure. In fact, ACP in pure water crystallizes into non-oriented HA nanoparticles (Fig. 1A). Conversely, when ACP is immersed in a solution of calcium and phosphates ions but in absence of fluoride octacalcium phosphate ($Ca_8H_2(PO_4)_6 \cdot 5H_2O$) platelets are formed [15,17].

Compression-molded ACP and Cit-ACP substrates exhibit a flat surface composed of rounded nanoparticles, approximately 50 nm in diameter, with no significant morphological differences between the two materials (Fig. 1A, upper row). After incubation in water, both substrates have a flat surface composed by unoriented elongated nanocrystals, approximately 100 nm long and 20–50 nm wide, due to water-mediated crystallization of ACP or Cit-ACP into HA (Fig. 1A, middle row). After incubation in GS, the ANS is formed onto ACP and Cit-ACP substrates (Fig. 1A, bottom row). The formation mechanism was elucidated in previous works; in brief, the presence of F^- ions combined with ACP's high reactivity and dissolution induces the formation of elongated FA nanocrystals onto ACP. During their growth, FA nanorods self-align perpendicularly to the substrate surface, forming the oriented array of nano-needles, as "vertical" is the only available growth direction [15]. In the case of the Cit-ACP substrate, the dissolution of the nanoparticles releases citrate anions in GS; these ions adsorb to the newly-formed FA nanorods, inhibiting their growth [15]. As consequence, the crystals grown onto Cit-ACP substrate are thinner, less crystalline, and less oriented as nano-needles (Fig. 1B) than those on ACP substrate. Here we further demonstrate that the crystal growth inhibiting effect of citrate is inversely proportional to substrate molding pressure (Supplementary Fig. 1). Cit-ACP 800 MPa substrate produces an ANS morphology similar to ACP GS, while at molding pressure of 37 MPa the ANS is not formed due to strong inhibition effect of citrate. We correlated this trend to citrate release from Cit-ACP substrate (Supplementary Fig. 2) as high-

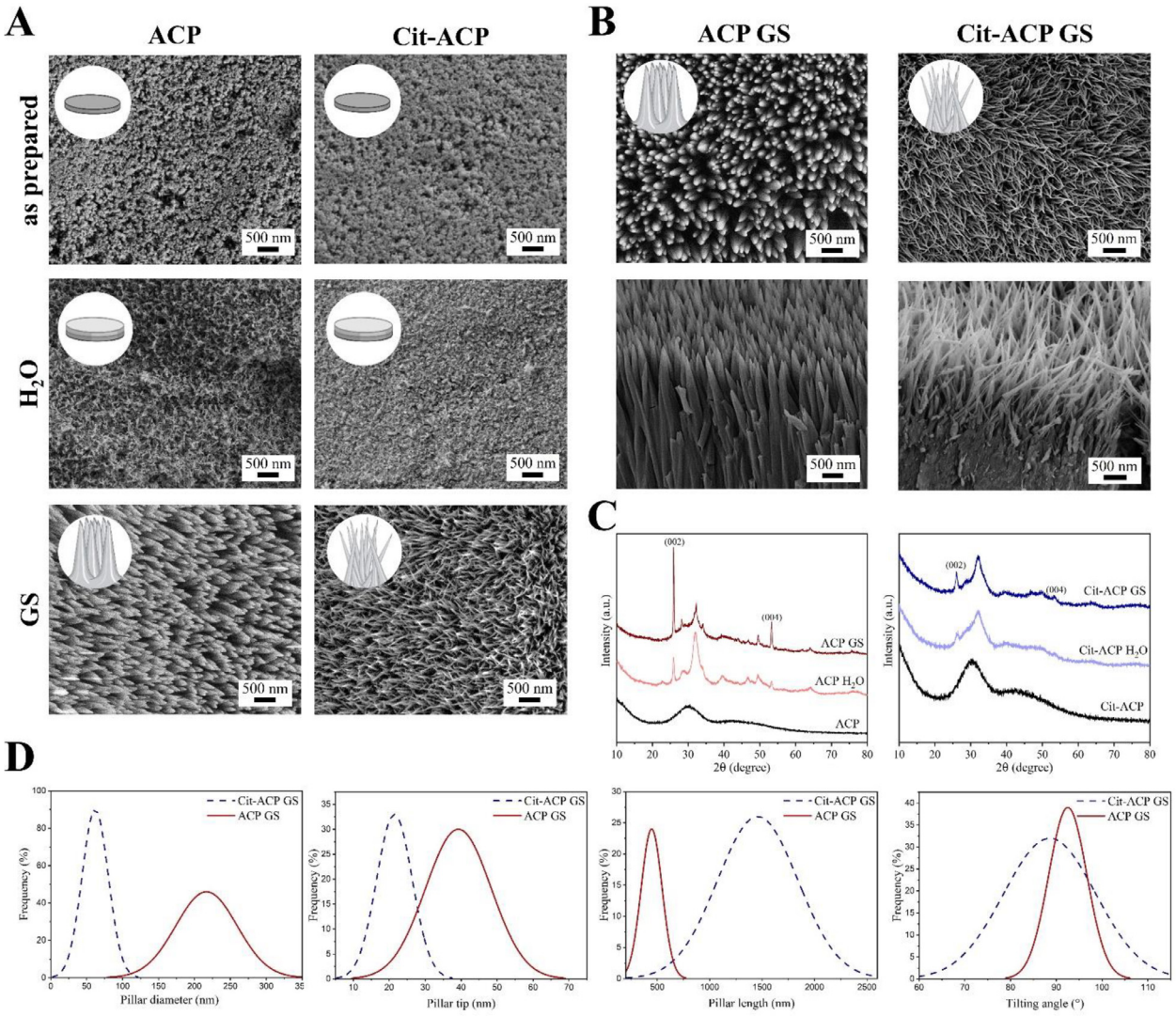

Fig. 1. Morphology, crystallinity, and morphological parameters of ANSs grown onto ACP. (A) Top-view SEM micrographs of ACP and Cit-ACP substrate surfaces after molding at 137 MPa (as prepared), after 24 h of incubation in water at 37 °C (H_2O), or after 24 h of incubation in GS at 37 °C (GS). (B) SEM micrographs of the ANSs of ACP GS and Cit-ACP GS (top row) and their respective cross-sections (bottom row). (C) XRD patterns of ACP (left) and Cit-ACP (right) before and after 24 h of incubation in water or in GS for at 37 °C. (D) Gaussian fitting of morphological features of ACP GS and Cit-ACP GS topographies measured by FEG-SEM. From left to right: needle diameter, needle tip diameter, needle length, needle angle with respect to the surface.

pressured, denser, and less porous substrates have a lower citrate release compared to less-compacted substrates. On the other hand, the formation of ANS onto ACP immersed in GS is independent of molding pressure (Supplementary Fig. 2). Considering this finding, in this work we focused on the ANSs obtained from substrates formed with 137 MPa of molding pressure, referred to thereafter as ACP GS and Cit-ACP GS.

The crystalline nature of the arrays of nano-needles was investigated by XRD (Fig. 1C). XRD patterns of ACP and Cit-ACP substrates before incubation are similar and do not present any diffraction peak, proving their amorphous nature. On the other hand, the XRD patterns of ACP GS, Cit-ACP GS, and their negative controls incubated in water (identified as ACP H_2O and Cit-ACP H_2O) all show diffraction peaks, attributed to crystalline apatite phase. The presence of these peaks indicates that incubation with GS or water induced the crystallization of ACP in an apatitic phase, either by direct crystallization of ACP or by epitaxial growth of the nano-needles. However, XRD patterns do not allow distinguishing whether this phase is hydroxyapatite or fluorapatite, as peak resolution is low and the two phases differ only by approximately 0.05 Å in *a-b* cell axis length [34]. For ACP GS and Cit-ACP GS, diffraction peaks are higher, and sharper compared to ACP H_2O and Cit-ACP H_2O, respectively. The same holds when comparing ACP samples to the corresponding Cit-ACP ones. In particular, the (002) peak at 25.9° and the (004) peak at 53.2°, highlighted in Fig. 1C, are even higher and sharper in the case of ACP GS sample, revealing a crystalline preferred orientation with the c-axis perpendicular to sample surface. Previous works support that HA nanocrystals grow along the crystalline *c*-axis [35], thus the preferential orientation in this direction indicates that the nano-needles are in an ordered structure parallel one to the other. The intensity of preferential orientation effect is correlated to the uniformity of nanocrystals array, thus the higher intensity of (00*l*) peaks for ACP GS in comparison to Cit-ACP GS confirms that ACP GS nano-needles are more ordered than Cit-ACP GS ones. Finally, the broader and less defined HA peaks for Cit-ACP GS and Cit-ACP H_2O compared to their ACP counterparts indicate a lower crystallinity and proving that citrate has inhibited the crystal growth.

SEM micrographs of ANS of ACP GS (Fig. 1B, left) show highly oriented thick nano-needles. The needles are ≈ 200 nm wide and

gradually become narrower on their tips, down to 30–50 nm. Micrographs of sectioned samples show that the crystals are almost perpendicular to the substrate and are several micrometers long. Overall, the overgrown layer is approximately 10 μm thick and is constituted by tightly packed nanocrystals, as shown by low-magnification micrographs (Supplementary Fig. 3). In contrast, the topography of ANS of Cit-ACP GS is made up of thin, less oriented, and less densely packed nano-needles (Fig. 1B, right). Cit-ACP GS nanoneedles have a diameter of ≈ 100 nm and become narrower at the tips. Cross-section micrographs show that these crystals are shorter (the overgrown layer is <4 μm thick) and less aligned (Supplementary Fig. 3). The morphological parameters of ANSs were studied through image analysis (Fig. 1D). The thicker nanocrystals of ACP GS have an average diameter of approximately 210 nm (with a diameter in the range 100 - 300 nm), while those of Cit-ACP GS were thinner (with an average diameter of approximately 60 nm) and have a narrower size distribution (20 - 100 nm) (Fig. 1D, left). Both ACP GS and Cit-ACP GS nanocrystals wear thin in the tips, with a tip diameter of 35 ± 15 nm for ACP GS and 20 ± 6 nm for Cit-ACP GS, (Fig. 1D, middle-left). Regarding needle length, Cit-ACP GS has an average length of 1.4 μm and spans from 0.8 to 1.8 μm (measured from the top of the rod to its base, as schematized in Supplementary Fig. 4) (Fig. 1D, middle-right). In the case of ACP GS, the length of the needles is of several microns, but they are densely packed without voids at their base (see Supplementary Fig. 3). This is an important feature, as the bactericidal action of ANSs is attributed to the mechanical strain between bacterial membrane regions in contact with the needles and those that are suspended, therefore voids between nano-features are essential [5]. For this reason, in "needle length" measurement of ACP GS we considered as "bactericidal region" only the top part of the overgrown layer, where the needles are thin and less packed (as schematized in Supplementary Fig. 4). With this assumption ACP GS nano-needles resulted to be shorter than Cit-ACP GS, with an average length of 0.4 μm and a range between 0.2 to 0.8 μm (Fig. 1D, middle-right). Finally, the measurement of needle inclination showed that the nanocrystals were almost perpendicular to substrate surface for both ANSs, with a limited deviation for ACP GS (± 10°) and a broader tilting for Cit-ACP GS (± 25°) (Fig. 1D, right).

We have compared the morphological parameters of the ANSs prepared in this work with those reported in the study by Iglesias-Fernandez et al. [18], which is one of the first papers on CaP-based ANSs obtained through a bottom-up approach. In this study, the nano-needles were grown by the hydrolysis of compression molded disks of α-tricalcium phosphate (α-$Ca_3(PO_4)_2$) either through hydrothermal treatment (120 °C, 2 atm, 30 min) or by immersion in water for a long time (37.5 °C, 1 atm, 7 days) and were proved to be effective against Gram-negative bacteria. In comparison, our ANSs formed with a simpler and biomimetic process have a thinner needle tip (Cit-ACP GS) but a broader base. They also exhibit a comparable needle height and have a narrower tilting angle distribution. The bactericidal effect of ANSs is widely reported, but there is little information on the correlation between morphological features of ANSs and optimal antibacterial activity. In the meta-analysis of natural and synthetic ANSs reported by Linklater et al., it can be inferred that the bactericidal effect of ANSs is achieved when the nano-needles have a height of 100–900 nm, a tip diameter of 20–200 nm, and a spacing of 10–400 nm [13]. A more narrow size range suitable to kill Gram-negative bacteria is provided by the systematic study on ANSs of polycarbonate by Cui et al. [36] and the literature meta-analysis of Iglesias-Fernandez et al. [18]. According to these sources, to achieve the best bactericidal effect, the nano-needles must have (i) a height higher than a critical threshold of ≈ 200 nm and lower than 1 μm, (ii) a tip diameter as thin as possible, at least < 60 nm, and (iii) an interpillar spacing between 100 and 200 nm. Therefore, the ANSs developed in this work possess all the structural characteristics necessary for high antibacterial activity.

Fragments of single nanocrystals were observed by TEM (Supplementary Fig. 5). At high magnification, it can be observed that both ACP GS and Cit-ACP GS nano-needles appear as cohesive structures and do not present sub-particles (Supplementary Fig. 5A). TEM micrographs confirm that the crystals are 200–300 nm wide at the base and progressively become thinner, ending with a tip that is <100 nm. Interestingly, the SAED patterns of the two samples are different (Supplementary Fig. 5A). ACP GS exhibits a well-ordered spot pattern, indicating a single crystal behavior, while the non-ordered spots of Cit-ACP GS indicate its polycrystallinity. Indexing of ACP GS SAED patterns collected at several tilting angles (Supplementary Fig. 5B) confirmed that the needle was a single crystal with an apatitic structure. The SAED pattern collected with the electron beam perpendicular to the nanocrystal's main axis (Supplementary Fig. 5A) corresponded to the [120] zone axis of apatitic structure. This confirmed that the nanoneedle's main axis was oriented along the crystalline *c*-axis. [37].

To obtain more structural information on ANSs, different X-ray diffraction techniques with specific sensitivities were employed. Specifically, to distinguish the different scattering contributions arising from the anisotropy and preferred orientations of nano-needles in ANSs, diffraction patterns were also collected by a 2D detector in grazing incidence (GIWAXS) and transmission (WAXS) geometry. The combination of GIWAXS and WAXS allows for probing both sample's surface and bulk, respectively, as well as crystal lattice planes with different orientations to sample surface. Indeed, while the XRD theta/2theta scan directly selects only the peaks related to the lattice planes with a preferred orientation parallel to film surface, GIWAXS patterns contain more structural information due to the large number of peaks visible along different azimuthal directions on the 2D detector. This allows fitting the entire diffraction pattern folded into a 1D profile, while also clearly highlighting the preferred orientations. GIWAXS 2D and relevant 1D-folded patterns are reported in Fig. 2A and 2B, respectively. GIWAXS patterns of ACP GS and Cit-ACP GS (top and middle rows) clearly demonstrate an increase of crystallinity of the topmost layers (i.e. the ANSs overgrowth) compared to ACP and Cit-ACP substrates (bottom row). This is evident from the well-defined diffraction rings/peaks observed for Cit-ACP GS and ACP GS. Furthermore, ACP GS is characterized by much sharper peaks (higher crystallinity) and uneven distribution of the diffracted intensity along the azimuth, indicating a high preferred crystallographic orientation. The same trend is observed in the WAXS (transmission geometry) patterns (Fig. 2C and 2D). However, these patterns more closely resemble the typical diffraction pattern of randomly oriented polycrystalline HA. Indeed, the patterns also represent the layer underneath the nano-needles, which is composed by non-oriented HA nanocrystals as reported previously [15]. Nevertheless, WAXS patterns collected at various positions in the sample (Fig. 2D) reveal, in some instances, unusual relative peak intensities. In these cases, the HA (030) peak has a higher intensity than expected for a randomly oriented powder. This anomalous intensity confirms the orientation of the *a*-axis parallel to the substrate surface and, consequently, the preferred orientation of the *c*-axis perpendicular to it. The local appearance or disappearance of such contributions is ascribed to the occurrence of both the Bragg condition (i.e., suitable tilt of the needles to the incoming X-ray beam for diffraction maxima) and the possible shadowing effect of neighboring needles. This latter factor depends on the local density of the needles per unit area, and on the exit angle of the diffracted beam. As a result, 2D WAXS patterns occasionally (e.g. Supplementary Fig. 6) show half rings in different azimuthal directions. Therefore, WAXS patterns contain diffraction contributions from the non-oriented HA

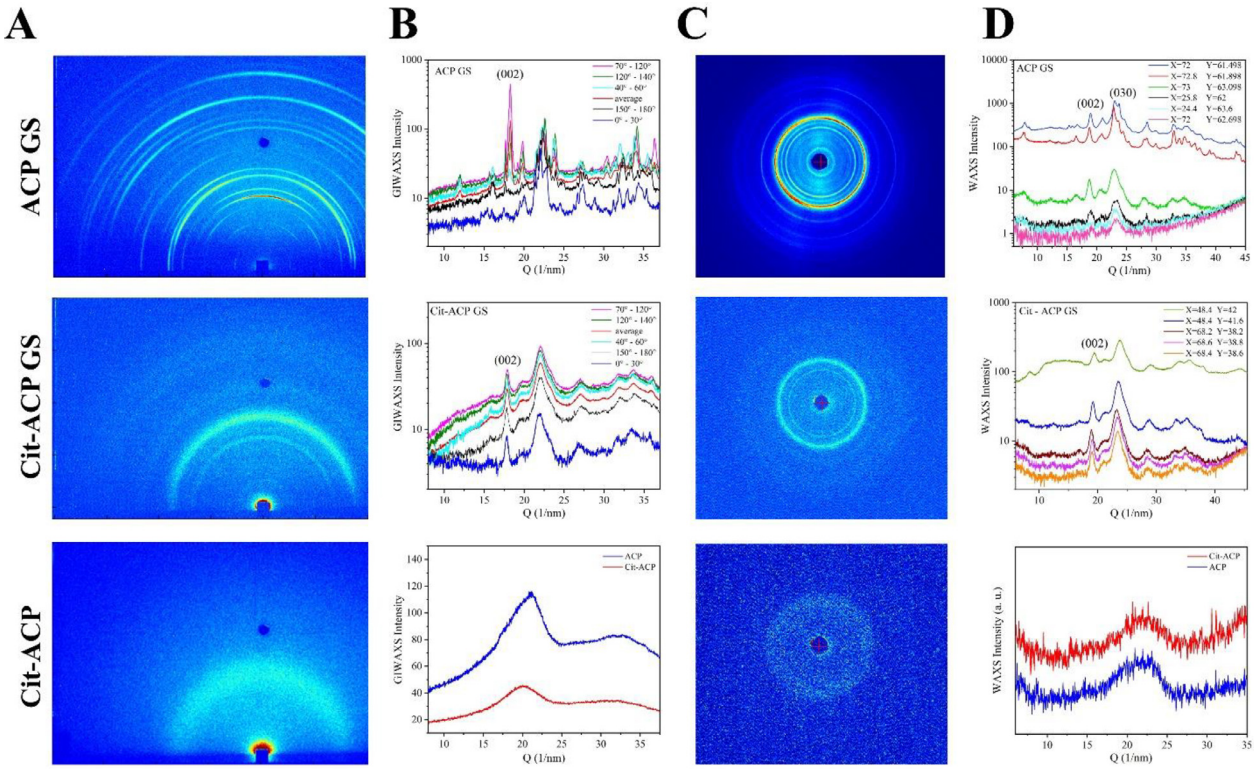

Fig. 2. Grazing incidence and transmission X-Ray diffraction of substrates and ANSs. (A) 2D and (B) relevant 1D-folded profiles of GIWAXS patterns of ACP GS, Cit-ACP GS, ACP (only 1D is reported), and Cit-ACP. For ACP GS and Cit-ACP GS, GIWAXS 1D cuts were extracted in different azimuthal sectors (where 0° and 90° directions represent parallel and perpendicular to the surface, respectively). (C) 2D and (D) relevant 1D-folded profiles of WAXS patterns of ACP GS, Cit-ACP GS, ACP (only 1D is reported), and Cit-ACP. For ACP GS and Cit-ACP GS WAXS patterns were collected at different sample positions, as indicated by the specific x and y coordinates.

nanocrystals below the ANSs as well as from the oriented needles, albeit to a lesser extent for the latter.

Quantitative results were obtained through whole profile fitting of WAXS and GIWAXS patterns of ACP GS and Cit-ACP GS (fits reported in Supplementary Fig. 7). For both samples, the patterns were fitted with hexagonal HA (database code ICSD 187,840) as unique crystalline phase in the sample, with unit cell parameters $a = 9.542$ Å; $b = 9.542$ Å; $c = 6.8832$ Å; $\alpha = \beta = 90°$; $\gamma = 120°$ WAXS patterns were fitted for both samples, whereas only ACP GS GIWAXS pattern was fitted, as Cit-ACP GS GIWAXS pattern showed no differences with the corresponding WAXS (Fig. 2). The crystalline domains derived from WAXS whole profile fitting of ACP GS are twice as large as those of Cit-ACP GS ones, in agreement with the dimensions of their respective growth layers. Crystalline domains aspect ratios (ratio between the maximum and minimum dimension, i.e. crystallite major and minor axes) derived from WAXS patterns are similar between ACP GS and Cit-ACP GS (about 1.6). These similar aspect ratios confirm that the main scattering contribution of WAXS patterns is derived from the non-oriented HA nanocrystals layer. In contrast, the aspect ratio calculated from ACP GS GIWAXS pattern is about 2, as GIWAXS captures the preferred (002) orientation as well as the anisotropic growth of the needles. Data collected at different sample positions in transmission geometry demonstrate the local homogeneity of the crystalline phase (Fig. 2D).

3.2. Antibacterial activity of ANSs

The bactericidal activity of ANSs was assessed against both Gram-negative and Gram-positive bacterial strains resistant to antibiotics. To evaluate the antibacterial efficacy of different surfaces, we conducted an adhesion-based assay to assess contact-killing designs [4]. PBS was utilized as the cell medium to ensure a consistent evaluation of bacterial viability on ANSs over time, maintaining stability in the number of attached populations throughout the experiment. In many studies evaluating the antimicrobial effectiveness of ANSs, a nutrient-deficient medium was intentionally selected [38,39]. This approach aims to promote microbial adhesion to the surface, mimicking the first phase of biofilm formation, which is a common virulence factor in prosthetic joint infections. A relatively short bacteria incubation period (4 h) was chosen to exclude any relevant mortality effect due to nutrient deprivation [40]. Moreover, PBS creates an isotonic environment that maintains bacterial cell wall and membrane physiology. We used a Live/Dead viability kit that relies on the absence or presence of bacterial wall damage to indicate bacterial viability. This factor is crucial in understanding the mechanism by which bacterial cells succumb to ANS-induced effects [3]. In detail, using this kit, viable cells with intact cell membranes were stained green (SYTO 9), while cells with damaged membranes were stained red (propidium iodide, PI), indicating non-viability. The Live/Dead kit enabled quantification of the total number of cells adhered to various substrates and the relative ratio of dead cells. As negative control, bacteria were incubated on flat ACP H_2O and Cit-ACP H_2O surfaces. Indeed, CaP materials can influence bacterial metabolism by altering the pH and ion concentration of the medium. Therefore, to decouple the biological response induced by ANSs' chemical composition from that induced by their nano-needle structure, the comparison was made with the non-nanostructured surfaces possessing comparable chemical composition.

Confocal microscopy micrographs of *P. aeruginosa* and *S. aureus* adhered onto ACP GS and Cit-ACP GS are reported in Fig. 3A-B. Live/Dead assay demonstrated that, after only 4 h of adhesion, both samples exhibited notable cytocidal activity against *P. aerug-*

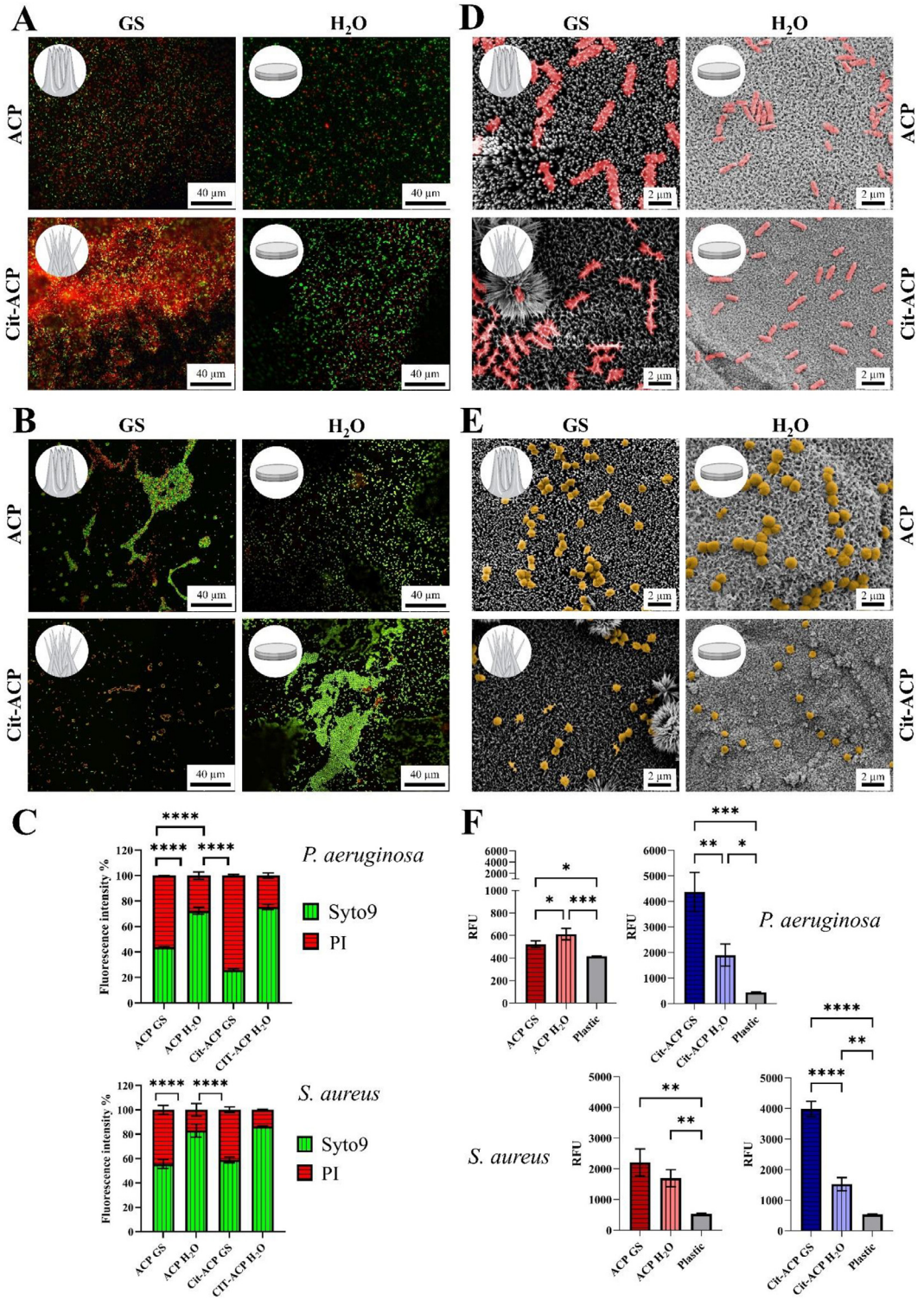

Fig. 3. Cell viability, morphology, and ROS generation of antibiotic-resistant bacterial strains adhered to ANSs. (A-B) Confocal microscopy micrographs of (A) XDR *P. aeruginosa* and (B) Methicillin-resistant *S. aureus* adhered to ACP GS, ACP H_2O, Cit-ACP GS, and Cit-ACP. Both bacterial strains were stained for Live/Dead assay; red cells correspond to bacteria with damaged membrane, green cells correspond to viable bacteria. When viable and damaged bacteria overlap, a yellow color is observed. (C) Quantitative analysis of Syto9 and PI fluorescence emission expressed as percentage of total fluorescence emission. The bactericidal action of the different ANSs (viable and dead cell density) is compared to Live/Dead assay fluorescence emission. Data are expressed as mean ± standard deviation (n = 3 from 3 independent experiments). (D-E) SEM micrographs of (D) XDR *P. aeruginosa* and (E) Methicillin-resistant *S. aureus* adhered on ACP GS, ACP H2O, Cit-ACP GS, and Cit-ACP H2O. *P. aeruginosa* cells are colorized in red, *S. aureus* in yellow. (F) Quantitative analysis of ROS release from for *P. aeruginosa* and *S. aureus* bacterial cells adhered for 4 h to ANS and flat surfaces. Data are expressed as mean ± standard deviation (n = 3 from 3 independent experiments).

inosa and *S. aureus*, showing an average bactericidal activity that was statistically significant when compared to that measured on flat ACP H_2O and Cit-ACP H_2O surfaces. All viability and adhesion data were quantified based on live/dead fluorescence signals and are presented in Fig. 3C. Cit-ACP GS demonstrated the highest bactericidal activity among the ANSs, causing 74.1 ± 0.9 % mortality of *P. aeruginosa* cells. ACP GS induced 56.1 ± 0.2 % of non-viable cells, indicating the death of around half of the adherent population (Fig. 3A,C). Conversely, ACP H_2O and Cit-ACP H_2O flat controls showed a statistically significant lower percentage of dead cells, with 28±3 % and 25±2 % of non-viable cells, respectively. Bacterial viability data against *P. aeruginosa* indicate that the thinner nano-needles of Cit-ACP GS were more bactericidal than the thicker nano-needles of ACP GS, as a small needle tip is critical for bactericidal activity [13]. In this regard, at comparable adhesion times both ACP GS and Cit-ACP GS have a superior bactericidal activity than the CaP-based ASN grown by hydrothermal hydrolysis by Iglesias et al., where a 35–45 % of dead cells against a non-antibiotic resistant *P. aeruginosa* strain is reported [18]. The higher efficacy of ANSs grown on ACPs might be due to their smaller needle tip diameter (20–30 nm for ACP GS and Cit-ACP GS vs 60 nm of the needles obtained through hydrothermal treatment).

The antibacterial activity against *S. aureus* (Fig. 3B-C) is lower than against *P. aeruginosa*. This result is consistent with literature which reports greater resistance of Gram-positive bacteria against similar surfaces [5,41]. Nevertheless, ACP GS and Cit-ACP GS exhibit significant bacterial mortality (44±4 % and 41±2 %, respectively), statistically different from negative controls (17±5 % and 14±1 % for ACP H_2O and Cit-ACP H_2O) with efficacy comparable to other types of ANSs [42-44]. *S. aureus* displays a less pronounced sensitivity to nano-needle morphologies in comparison to *P. aeruginosa*, as there is no significant difference in mortality between thinner or thicker nanorods.

Overall, our CaP-based ANSs have a significant antibacterial effect against both Gram+ and Gram- cells, especially considering that a short contact time was tested (4 h). Previous works have shown that for ANSs the amount of dead bacteria increases over contact time, tentatively attributed to bacteria rupture during cell division or to intracellular accumulation of ROS during the permanence onto nano-needles [18,45]. Therefore, for our ANSs, we anticipate a higher antibacterial activity for longer contact times, provided that the nanostructure is preserved.

The bactericidal effect of ANSs is thought to stem from either (i) the direct rupture of the bacterial membrane, resulting in the release of cytoplasm (occurring during cell adhesion to the nano-needles or when an adhered cell attempts to move or to divide), or/plus (ii) the induction of oxidative stress due to mechanical stresses imposed on the membrane [5,45]. To unravel the bactericidal mechanisms of our ANSs, we measured the release of reactive oxygen species (ROS) from bacterial cells, as ROS production is indicative of oxidative stress. ROS release was quantified after a 4-hours period of bacterial adhesion onto the ANSs, control surfaces, or bare plastic, as illustrated in Fig. 3F. Notably, irrespective of the bacterial strain, contact with Cit-ACP GS induced a significantly higher ROS release (*P. aeruginosa*4368 ± 764 RFU; *S. aureus*3980 ± 250 RFU) compared to both the Cit-ACP H_2O (*P. aeruginosa* 1898 ± 436 RFU; *S. aureus* 1525 ± 215 RFU) and bare plastic control (*P. aeruginosa* 435 ± 27 RFU; *S. aureus* 531 ± 24 RFU).This finding underscores the importance of the oxidative stress on the bactericidal mechanism for this particular ANS. The flat ACP H_2O (*P. aeruginosa* 612 ± 50 RFU; *S. aureus* 1697 ± 279 RFU) and Cit-ACP H_2O surfaces slightly increased ROS generation compared to plastic, suggesting a mild bactericidal effect even on a non-oriented apatite substrate, as suggested by others [18,46]. ACP GS (*P. aeruginosa* 523 ± 30 RFU; *S. aureus* 2208 ± 441 RFU) possessed a notably lower ROS production than Cit-ACP GS, yet significant differences were observed compared to plastic for both bacterial strains (Fig. 3F). Remarkably, with *P. aeruginosa,* ACP GS demonstrated even lower ROS generation than ACP H_2O. Given that ACP GS bactericidal activity is higher than that of ACP H_2O and approached that of Cit-ACP GS, we assume that ACP GS bactericidal action is likely independent of ROS generation and involves other mechanisms.

SEM microscopy was employed to assess the morphology of *P. aeruginosa* and *S. aureus* adhered to our ANSs, as illustrated in Figs. 3D and 3E. On ACP GS and Cit-ACP GS *P. aeruginosa* cells underwent significant bactericidal effects, exhibiting a distorted and deflated appearance (Fig. 3D). This pronounced alteration in cell morphology suggests membrane damage or rupture with the release of the inner content. In contrast, bacterial cells in negative controls remained plump and undamaged, confirming the integrity of their membranes. For both ANSs, the nano-needles penetrated the bacterial cells, and for Cit-ACP GS the needles appear bent due to bacteria adhesion. In the case of *S. aureus* (Fig. 3E), perforated and deflated cocci are observable on both ACP GS and Cit-ACP GS, although some intact cells are present. As evident in Fig. 4, high magnification micrographs better clarify the differential morphologies that *P. aeruginosa* and *S. aureus* can assume in response to perforation-associated mechanical stresses. As already stated, the Gram-negative bacteria demonstrate a marked morphological alteration between control and both ANSs (Fig. 4A), and protrusions of nano-needles are visible through the bacillus body, which appears pierced in several places. The Gram-positive coccus *S. aureus* appears as more resilient, even if is clearly damaged by ANSs (Fig. 4B). The micrographs taken from a lateral perspective of ANSs surfaces (Fig. 4C) enrich the morphological characterization, giving a tridimensional overview of the severity of cell-damage and showing the partial or complete cells deflation.

Overall, our results confirm that the CaP nano-needles arrays are bactericidal against both Gram-negative and Gram-positive bacteria. The antibacterial action of ACP GS and Cit-ACP GS against *P. aeruginosa* is based on bacterial membrane rupturing, deformation, or perforation after cell adhesion. Additionally, only for Cit-ACP GS the induction of oxidative stress due to mechanical deformation is a significant co-cause of death at longer incubation times. The thinner nano-needles of Cit-ACP GS have higher bactericidal activity compared to thicker ACP GS ones, suggesting that the smaller needle diameter is more efficient in killing *P. aeruginosa* as it induces both membrane damage and oxidative stress. As reported previously for other types of ANSs, Gram-positive *S. aureus* is more resistant to membrane rupturing, and thus, a lower bactericidal activity compared to *P. aeruginosa* is observed. There is a limited difference in bactericidal effect between thicker and thinner nano-needles, but also in this case Cit-ACP GS induces a significantly higher ROS generation in comparison to ACP GS. Considering these two factors together we hypothesize that against *S. aureus* the thicker nano-needles are more efficient in inducing membrane damage than the thinner ones, but the bactericidal activity of the latter is enhanced by higher induction of oxidative stress, obtaining at the end a comparable efficacy between the two ANSs.

3.3. Interaction of mammalian cells with ANSs

After establishing the bactericidal effectiveness of CaP-based ANSs, we verified their cytocompatibility with mammalian cells. For this preliminary evaluation, we used the VERO cell line, a widely recognized immortalized cell line often employed in cytotoxicity assays [47]. Cell viability was measured following a 24-hour incubation period, and an adhesion-based assay similar to the one applied to bacteria was employed, where viable cells with intact membranes were stained in green (calcein-AM), while dead

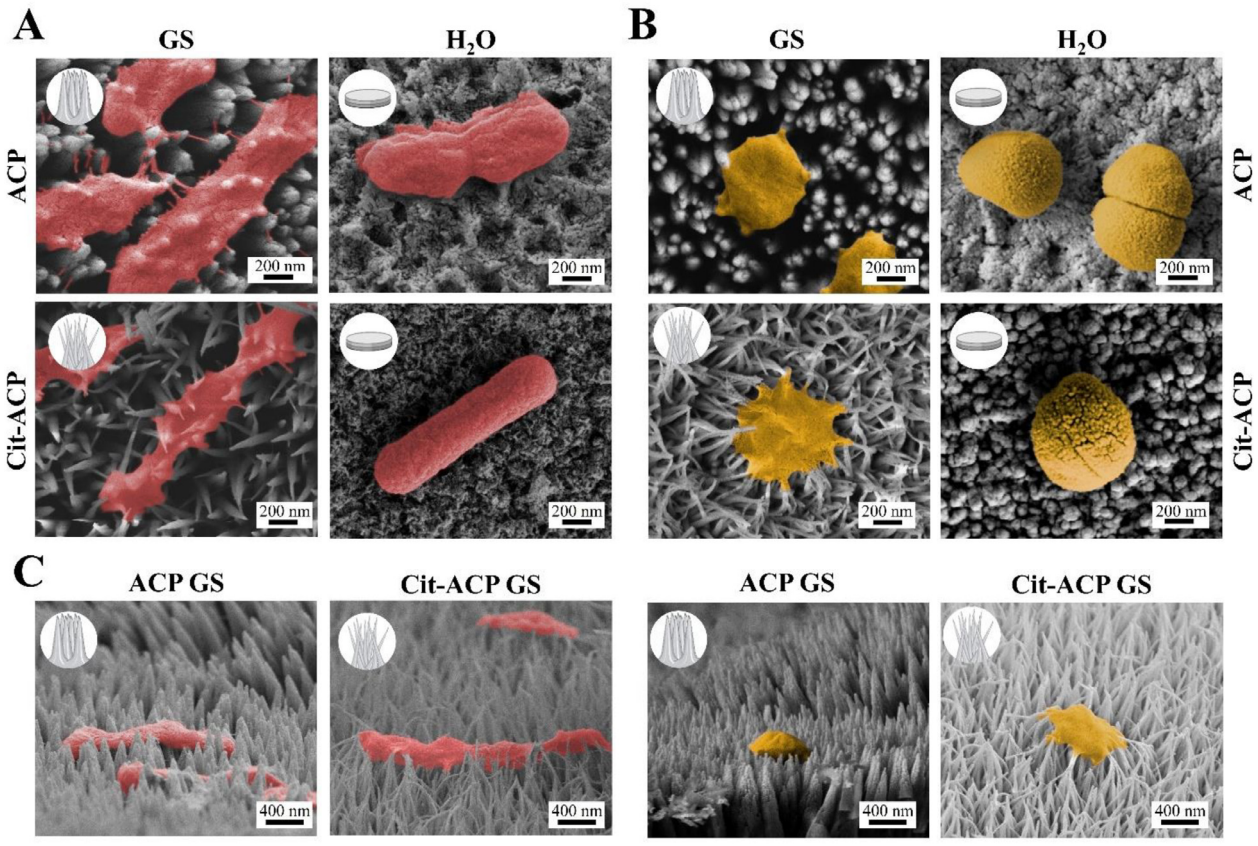

Fig. 4. Morphology of antibiotic-resistant bacterial strains adhered to ANSs at high magnification**.** SEM micrographs of (A) XDR *P. aeruginosa* and (B) Methicillin-resistant *S. aureus* adhered on ACP GS, ACP H_2O, Cit-ACP GS, and Cit-ACP H_2O. (C) Cross-section micrographs of *P. aeruginosa* and *S. aureus* adhered on ACP GS and Cit-ACP GS. *P. aeruginosa* cells are colorized in red, *S. aureus* in yellow.

cells with damaged membranes were stained in red (ethidium homodimer-1, EthD-1).

Fluorescence micrographs in Fig. 5A show VERO cells on samples with high viability and minimal dead cells. Fluorescence quantitative analysis (Fig. 5B) highlights that ACP GS, Cit-ACP GS and Cit-ACP H_2O have the highest cell viability of 79±2 %, 90±1 %, and 79±7 % respectively. Notably, ANSs exhibit superior cytocompatibility compared to flat controls (ACP substrate, p-value = 0.0287; Cit-ACP substrate, p-value = 0.0225), indicating enhanced cell proliferation. Even the ACP negative control, ACP H_2O, demonstrates robust cell viability at 68±3 %, highlighting the cytocompatibility of CaP-based materials. The significant difference between ACP GS and Cit-ACP GS suggests a more efficient VERO cell proliferation on thinner nanoneedles. Micrographs and cell coverage analysis show higher cell counts and a more uniform distribution on nanostructured surfaces, indicating that ANSs promote cell multiplication and spreading.

We examined cell morphology of VERO adhered to ANSs (Fig. 5C), revealing a clear distinction from flat controls. In ACP H_2O and Cit-ACP H_2O, cells clustered, formed few protrusions, and covered a limited surface. In contrast, ACP GS and Cit-ACP GS showed widespread and even cell spreading, preventing aggregate formation. SEM micrographs highlighted filaments and membrane protrusions attaching to the nano-needles, suggesting cells anchor to the nanostructured surface. Comparison with negative controls emphasizes the heightened bioactivity of nanostructured surfaces over biocompatible flat CaP surfaces. Enhanced cell colonization of ANSs due to nanostructure was previously observed in several bioinert materials, and it was hypothesized to be correlated to improved adhesion by nano-needles [7,48,49]. This anchoring, crucial for cell colonization and propagation on a bioactive surface, corroborate that our samples promote mammal cell proliferation [50].

The impact of ANSs on VERO cells was also evaluated by examining potential oxidative stress and membrane damage. The quantification of ROS release (Fig. 5D) reveals that both ANSs result in lower ROS generation compared to the control group on bare plastic, with Cit-ACP GS demonstrating particularly reduced ROS production. In contrast, flat controls exhibit a ROS production comparable to the baseline level on plastic substrate. These interesting results strongly suggests that when VERO cells adhere and spread on ANSs surfaces their oxidative stress undergoes a notable reduction compared to the conventional plastic or flat substrates. Significantly, this effect can be traced back to the distinct features inherent in the ANSs. Notably, the thinner and less oriented Cit-ACP GS demonstrated a superior ability in keeping ROS levels low compared to its ACP GS counterpart.

These preliminary analyses indicate a promising high cytocompatibility of CaP-based ANSs towards mammalian cells. The ANSs nanostructures promote cell adhesion, spreading, and decrease oxidative stress, parameters that suggest a propensity for being an optimal surface for mammalian cell colonization. There is a significant difference with flat controls, which are cytocompatible but not optimal for colonization, as cells tend to aggregate with each other. Our data indicate that nano-needle morphological parameters are relevant for VERO cells colonization, as the highest cell viability and lowest oxidative stress are achieved with thinner and less ordered nanocrystals.

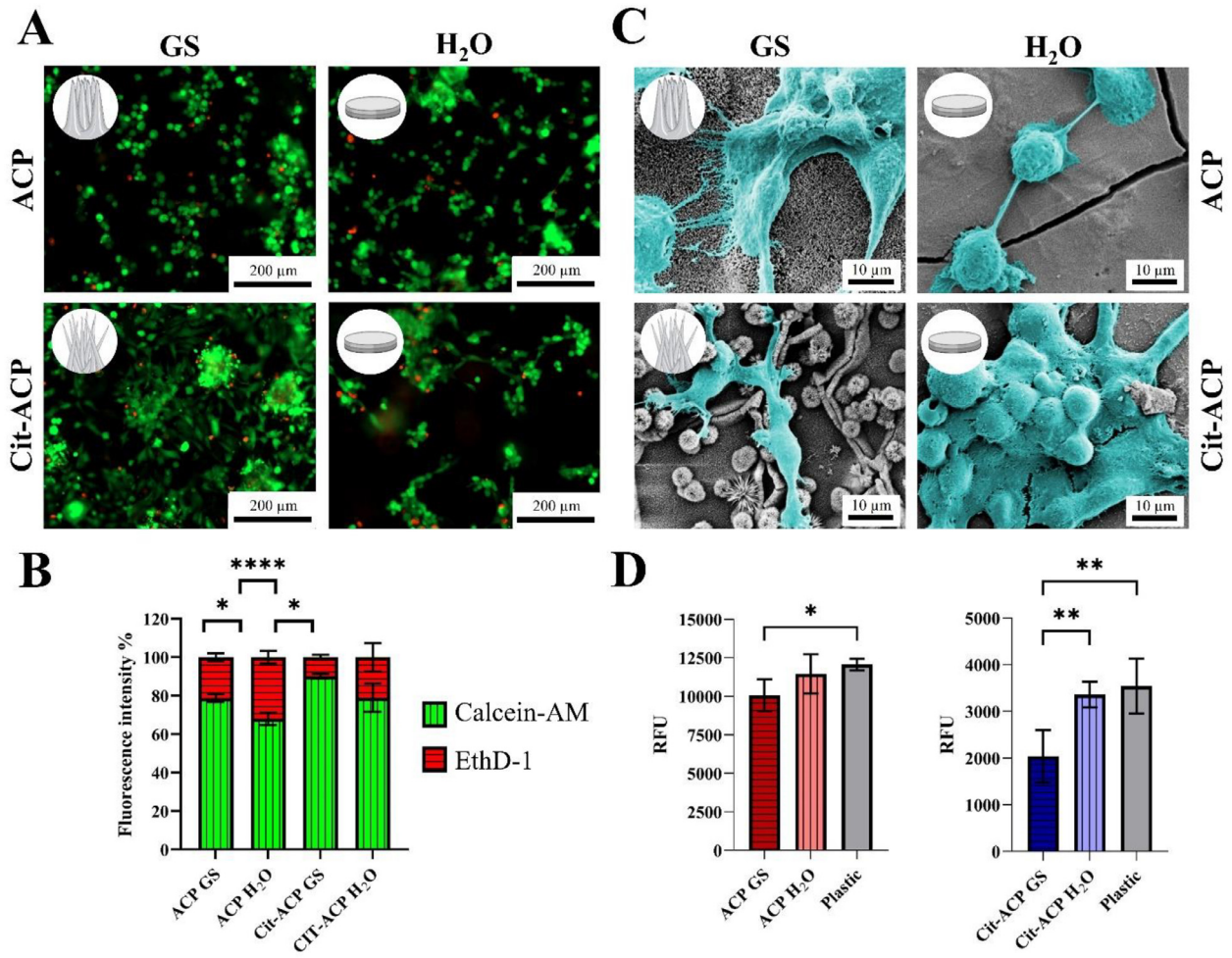

Fig. 5. Cell viability, morphology, and ROS generation of VERO cells adhered to the ANSs. (A) Confocal microscopy micrographs of VERO cells adhered to the ANSs for 24 h and stained with Live/Dead assay. Green cells represent viable cells, while red cells indicate dead cells. (B) Quantitative viability analysis and cell coverage on the ANSs. The data show the percentage of viable and dead cells compared to total cells. Data are expressed as mean ± standard deviation ($n = 3$ from 3 independent experiments). (C) SEM micrographs of VERO cells adhered to the ANSs; cells are colorized in light blue. (D) Quantitative analysis of ROS release from VERO cells adhered to the ANSs for 24 h. Data are expressed as mean ± standard deviation ($n = 3$ from 3 independent experiments).

3.4. Interaction of Adipose-derived Mesenchymal Stem Cells with ANSs

After proving the cytocompatibility of ANSs with mammalian cells, we proceed to test the materials *in vitro* with Adipose-derived Mesenchymal Stem Cells (Ad-MSCs), assessing cytocompatibility, cell-material interaction, and their potential to induce the expression of osteogenic-related genes. These tests aim to provide a preliminary evaluation of ANSs as substrates to potentially support local bone tissue regeneration following infection resolution at the damaged site.

Human Ad-MSCs were cultured on ANSs for a total of 14 days under specific osteogenic media conditions. This well-established model is favoured for its ease of access, trilineage differentiation potential, and suitability for *in vitro* bone tissue regeneration evaluation [21,22,51]. Cell-material interactions were firstly analysed in terms of cell proliferation, viability, and cell morphology.

The Presto Blue viability results shown in Fig. 6A clearly demonstrated that both ACP GS and Cit-ACP GS are significantly more bioactive compared to the flat surfaces of ACP H_2O (p value ≤ 0.0001) and Cit-ACP H_2O (p value ≤ 0.01), respectively, used as controls. This indicates that the nano-needle structures play a crucial role in modulating Ad-MSCs viability and proliferation [52].

Looking in detail at the cell viability, it was observed that ACP GS shows overall the best bioactivity in respect to the other samples, as it presents a statistically significant higher cell viability compared to both controls starting from day 2 of culture (Supplementary Table 2) and compared to Cit-ACP GS starting from day 7 (Supplementary Table 2). Notably, also Cit-ACP GS induces a statistically significant higher cell viability compared to its control (Cit-ACP H_2O) at day 3 and 7, but this induction seems to drastically disappear starting from day 10 (Fig. 6A and Supplementary Table 2).

Focusing on the proliferative potential, it was observed that Ad-MSCs cultured on ACP GS exhibited significant growth at all experimental time points (p value ≤ 0.001). This robust trend was not observed for the other tested samples. In fact, in ACP H_2O, Cit-ACP GS, and Cit-ACP H_2O only an initial growth occurred, resulting in a significant difference on day 1 and 2. Subsequently, the proliferative trend reached a plateau, followed by a decrease on day 7 for the control samples and on day 14 for Cit-ACP GS (Supplementary Table 3).

The qualitative evaluation of cell viability at day 1 by LIVE/DEAD assay (Fig. 6B) confirmed the Presto Blue analysis data. In summary, cell viability was confirmed on all surfaces, with mostly green live cells and few red dead cells observed. However,

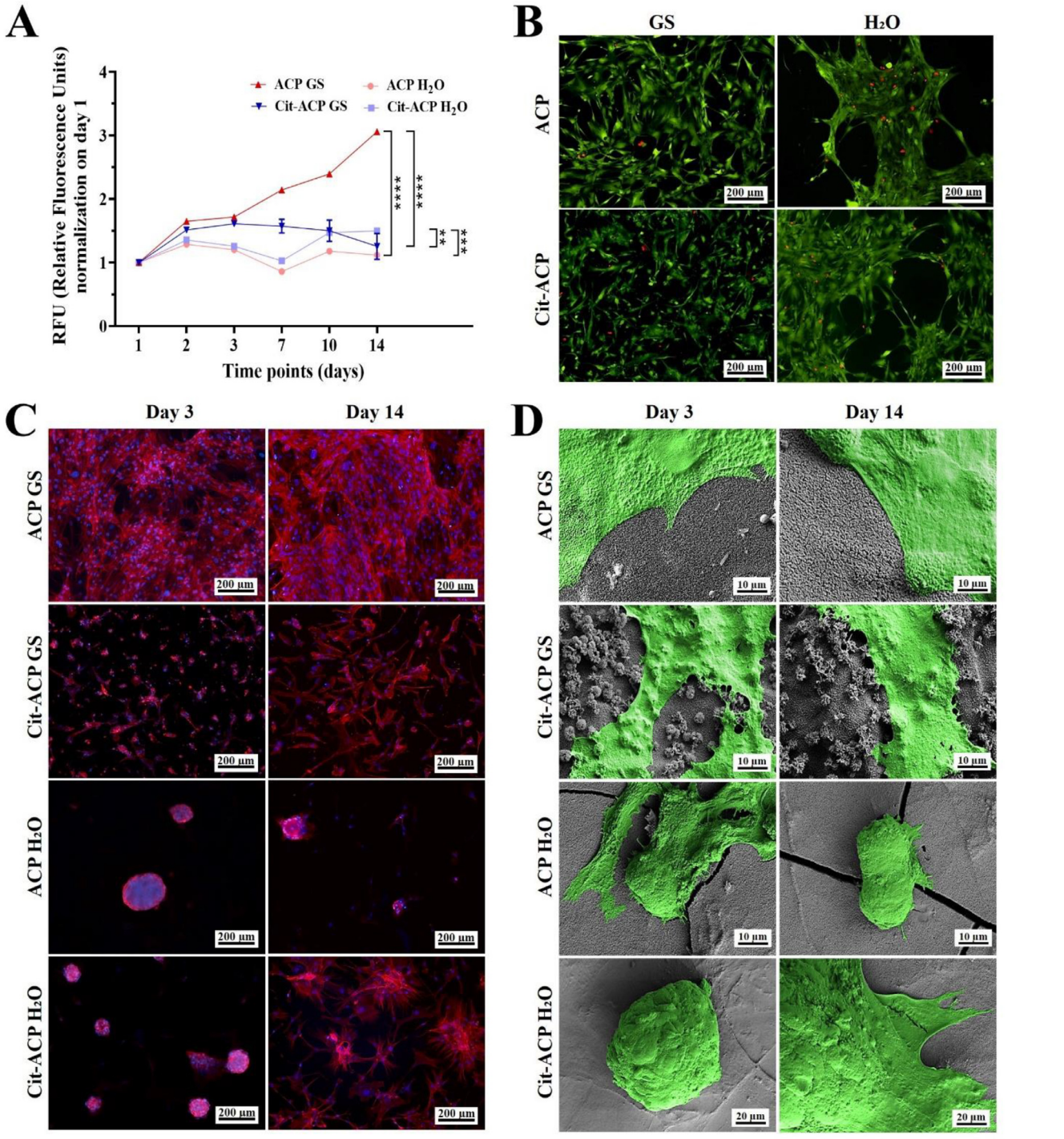

Fig. 6. Cell proliferation, viability, and morphology of human Ad-MSCs cultured onto ANSs. (A) Cell proliferation measured by Presto Blue™ Cell viability reagent. The RFU data normalization on day 1 (mean ± SEM) are presented in the graph. Statistically significant differences between ANSs and the controls are indicated in the graph: ** = p value ≤ 0.01, *** = p value ≤ 0.001 and **** = p value ≤ 0.0001. (B) Fluorescence microscopy of Ad-MSCs at day 1 stained with LIVE/DEAD viability assay. Live cells are shown green, dead cells in red. (C) Fluorescence microscopy of Ad-MSCs at day 3 and day 14 stained with actin and DAPI. The cytoskeleton is shown in red and cell nuclei in blue. (D) FEG-SEM micrographs of Ad-MSCs at day 3 and day 14. Ad-MSCs are colorized in green.

a slight increase in cellular aggregates was noted for both flat controls. The LIVE/DEAD assay also indicated a distinct morphology behaviour when cells were cultured on ANSs compared to flat surfaces, which was further examined in detail through morphological analysis. Fluorescence micrographs with actin and DAPI staining and FEG-SEM micrographs (Fig. 6C and D, respectively) of the Ad-MSCs at day 3 and 14 of culture clearly confirmed that, compared to flat surfaces, Ad-MSCs grown on ANSs exhibited an elongated shape with long cytoplasmic protrusions. This morphology is indicative of excellent cell adhesion and is considered a healthy appearance, supporting the widely reported role of ANSs in promoting such cell behaviour [52,53]. Moreover, cell elongation suggests that Ad-MSCs were able to accommodate the deformation stresses imposed by the nano-needles, likely due to their larger dimensions and more elastic membrane compared to bacteria (Fig. 6C and D) [18]. The evaluation of cell morphology also revealed a

notable difference between the two ANS surfaces. While a dense cellular layer was observed on ACP GS after just 3 days of culture, a lower number of cells was observed on Cit-ACP GS at both time points (Fig. 6C). In contrast, cells grown on the flat control surfaces tended to aggregate, resulting in a non-uniform distribution and limited anchoring points (Fig. 6C and D).

SEM analysis also allowed for the observation at a higher magnification of the interaction between Ad-MSCs and the nanostructured surfaces in terms of cell-nanoneedle contact points (Supplementary Fig. 8). Micrographs showed the ability of cell membrane to stretch and distort following the shape of the nano-needles without disrupting the cytoplasm, suggesting that the nanostructures may provide anchoring points for cell adhesion (Supplementary Fig. 8 and Fig. 6D).

The SEM micrographs of Supplementary Fig. 8–9 depict the evolution of the ANSs during incubation in osteogenic media. While the morphology of the samples on day 3 is comparable to pristine materials, by day 14, distinctions emerge between ACP GS, Cit-ACP GS, and their flat counterparts (Supplementary Fig. 8E,F and Supplementary Fig. 9A,B). Specifically, ACP GS at day 14 exhibits a smooth surface due to a layer of acicular nanoparticles (Supplementary Fig. 8E and Supplementary Fig. 9A). These nanoparticles, measuring approximately 20–40 nm in width and 60–100 nm in length, adhere and conceal ACP GS nano-needles, filling the voids between the crystals and forming a 150–200 nm thick cohesive layer (Supplementary Fig. 9E). In contrast, for Cit-ACP GS at day 14 the nano-needles can still be observed but are thicker and interconnected by acicular nanoparticles, creating a net-like structure (Supplementary Fig. 8F and Supplementary Fig. 9B). Notably, these alterations are unrelated to cellular activity, as cell-free ANS samples at day 14 present the same morphology (Supplementary Fig. 9). Conversely, the flat ACP H_2O and Cit-ACP H_2O samples do not display such nanoparticle deposits (Supplementary Fig. 8 G,H and Supplementary Fig. 9C,D,G,H). It is probable that these deposited nanoparticles result from the nucleation of calcium and phosphate ions present in the cell medium onto nano-needles, forming CaP nanocrystals. This phenomenon is pronounced in ANS samples due to the high exposed surface area. Therefore, the data indicate that the ANSs are stable and do not get degrade in cell medium. However, over a longer timeframe, the formation of a new mineral phase on them might alter the physical effects of nanostructure.

To elucidate the various morphological behaviours observed, we conducted immunofluorescence analysis of specific cell adhesion molecules (Fig. 7A). Cell adhesion molecules play a pivotal role in regulating cellular anchoring, shape, motility, and, consequently, cell survival, proliferation, migration, and differentiation. It is widely acknowledged that cell adhesion primarily occurs through the activation of transmembrane integrin molecules by extracellular matrix (ECM) ligands. This activation initiates a series of intracellular signalling events that ultimately lead to the reorganization of the actin cytoskeleton. In particular, the integrin activation is facilitated by cell-substratum contact sites known as focal adhesions (FA). These sites contain an array of proteins, such as Focal Adhesion Kinase (FAK), Paxillin, Vinculin, Talin, and others which co-cluster with integrin at cytoplasmic tails level in adherent cells. This clustering provides a structural link to the actin cytoskeleton [54,55]. The principal components of FA, namely FAK as non-receptor tyrosine kinase [56], and Paxillin as FAK partner that recruits diverse actin-binding proteins into a FA-cytoskeleton anchoring complex [57], were investigated using immunolocalization fluorescence microscopy (Fig. 7A). Micrographs revealed a distinctive “point-like” positivity of both FAK and Paxillin in ANSs, particularly in ACP GS, confirming that the nano-needle surfaces can initiate and reinforce the cell adhesion process (Fig. 7A). The heightened involvement of cell adhesion molecules observed in ANSs compared to the controls suggest that ANSs may expose cells to external mechanical forces, leading to an increase in FA points, as reported in various studies [58-60].

Indeed, the involvement of FA, specifically FAK [56,60] and Paxilin [57,61], in mechano-sensitivity to extracellular cues has been extensively demonstrated in various settings. This results in an overall increase in focal adhesions [58-60], which counterbalances the forces acting on the cell, causing changes in the cytoskeleton that can activate or deactivate downstream signalling pathways [62]. The cell shape, adhesion and actin organization of the cytoskeleton are intricately linked to the topographical design of the substrate, consequently affecting the cellular ability to colonize surfaces and proliferate. Specifically, nano-topographical features enhance cell anchoring and spreading compared to flat surfaces [63] due to the multiple extrinsic and intrinsic forces they exert on cells [62]. Preliminary systematic studies indicate that nanometric ANS needle tips induce the formation of focal adhesion points and substrate adhesion, and closely packed nanoneedles facilitate cell spreading and colonization, particularly for MSCs, aligning with our findings [64].

Our experimental data on both Ad-MSC and VERO cells consistently show enhanced cell adhesion, colonization, and proliferation on ANS surfaces compared to the flat surfaces. Literature on CaP materials has associated *in vitro* cell adhesion with various surface parameters, such as micro- and nano-roughness [65-67]. Morphological analysis suggests that our ANSs have higher microroughness compared to flat controls. However, current technology does not allow for a quantitative assessment of ANSs roughness, limiting the comparison to a qualitative evaluation.

The expression of genes involved in the early stages of osteogenic differentiation of Ad-MSCs was also analyzed with the final aim of investigating ANSs as a potential guide for damaged bone tissue regeneration after the resolution of the infection (Fig. 7B) [68-70]. After 7 days of culture an upregulation of RUNX-2 induced by both ANSs and controls has been reported, with statistical significances in ACP H_2O (fold-change 3.728), Cit-ACP H_2O (fold-change 4.190, p value $\leq$ 0.01), and Cit-ACP GS (fold-change 4.612, p value $\leq$ 0.001), compared to the cells grown in standard plastic culture systems used as internal control for the mRNA relative quantifications (referred to as “cells only”). The trend of RUNX-2 upregulation was observed on all tested surfaces at 14 days of culture compared to cells only, although no significant differences were reported. This suggests the commitment of Ad-MSCs to osteogenic lineage and confirms the well-known bioactivity of CaP in terms of osteoconductivity and osteoinductivity of stem cells (Fig. 6B) [71].

It is noteworthy that at day 7 RUNX-2 is significantly upregulated in Cit-ACP GS (fold-change 4.612) compared to ACP GS (fold-change 2.467, p value $\leq$ 0.05). In contrast ALP is statistically significantly upregulated in ACP GS (fold-change 4.752) compared to Cit-ACP GS (fold-change 0.5690, p value $\leq$ 0.001) as well as compared to the controls ACP H_2O (fold-change 2.622) and Cit-ACP H_2O (fold-change 2.964, p value $\leq$ 0.05). These findings align with the well-established roles and timing of gene expression pathways of these genes [68,69]. Indeed, during the early osteogenic process, RUNX2 functions as a transcriptional downstream activator of signalling molecules, including bone morphogenetic protein (BMP), crucial for osteoblast differentiation [68,69]. In this phase, cells initiate the synthesis of ECM, primarily composed of collagen type I. Subsequently, cells produce ALP and various non-collagenous proteins, followed by induction of ECM calcification [70]. Confirming previous reports, the expression of BMP-2 follows the expected profile. The results show a slight upregulation trend of BMP-2 at both time points, specifically in Cit-ACP GS (fold-change 2.547 and 1.743 at day 7 and 14, respectively), even though no statistically significant differences were observed. This suggests its interplay

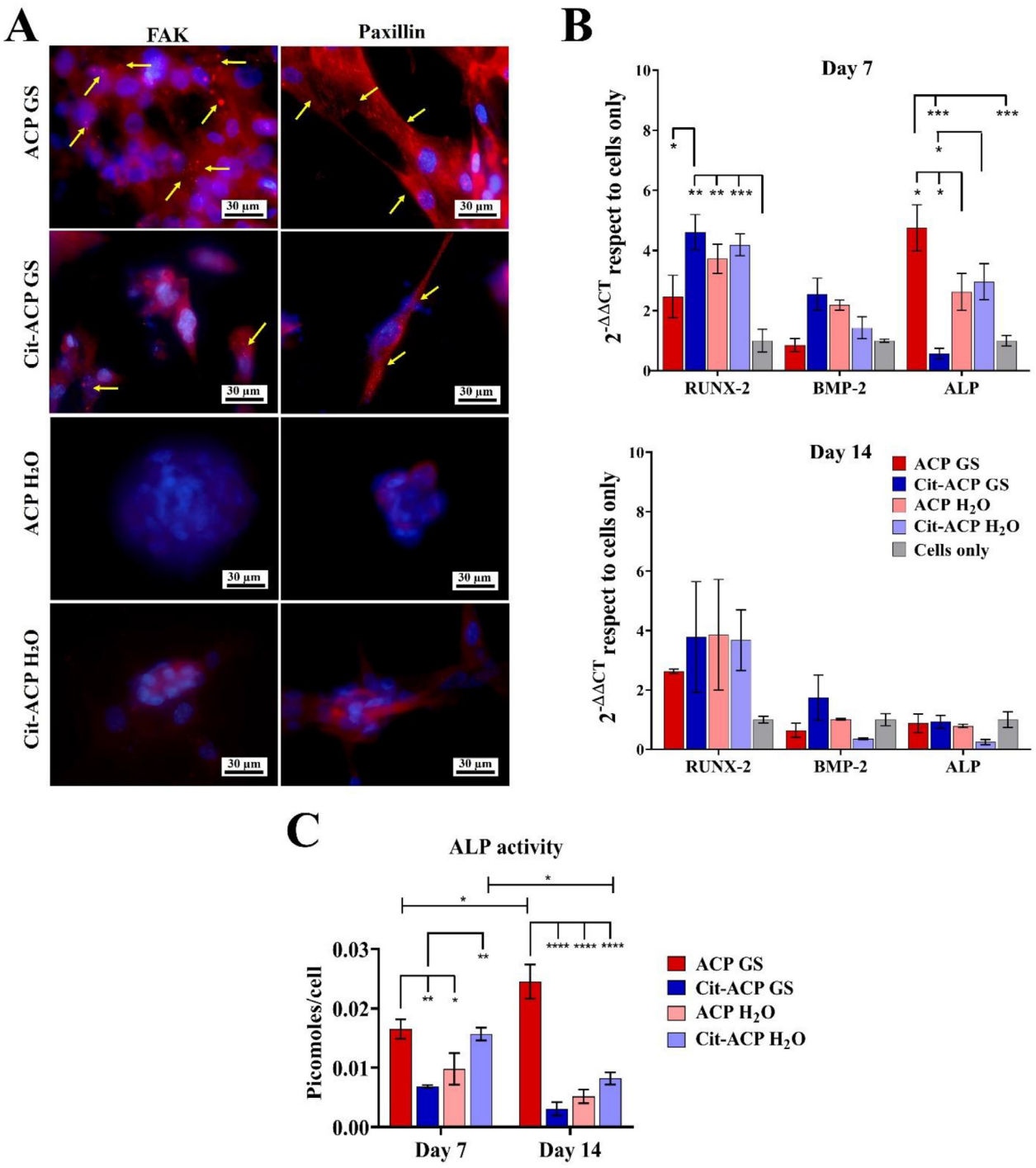

Fig. 7. Cell adhesion, gene expression and ALP activity of human Ad-MSCs adhered to ANSs. (A) Immunofluorescence microscopy of FAK and Paxillin adhesion markers at day 3 of culture. Positivity is shown in red and cell nuclei in blue. (B) Gene expression of osteogenic markers by Real Time PCR. The data are presented as $2^{-\Delta\Delta ct}$ fold-change with respect to cells only (mean ± SEM). (C) Quantification of ALP enzyme by p-nitrophenyl phosphate (pNP-PO_4) hydrolysis-based assay. The data are reported as picomoles of p-nitrophenol liberated per cell ± SEM. Statistically significant differences among samples are indicated in the graph as follows: * = p value ≤ 0.05, ** = p value ≤ 0.01, *** = p value ≤ 0.001 and **** = p value ≤ 0.0001.

role with RUNX-2 in the early commitment of MSCs in the osteogenic differentiation process (Fig. 7B).

The results support the notion that ACP GS exerts an earlier bioactive effect compared to the other samples, enabling the observation of an overexpression of genes related to later stages of differentiation as early as 7 days (Fig. 7B).

The expression of ALP appears to be downregulated in all the samples after 14 days compared to the expression at day 7. This is consistent with the expected expression trend observed for this gene in the osteogenic pathway, characterized by the activation and deactivation of ALP expression over a defined time of commitment [72].

To better understand the osteogenic potential of ANSs, ALP enzymatic activity was quantified (Fig. 7C). Significant activation was observed starting from day 7 in ACP GS, compared to Cit-ACP GS (p value ≤ 0.01) and both flat surfaces (p value ≤ 0.05 and ≤ 0.01).

Enzyme activity significantly increased until day 14 compared to day 7 (p value $\leq$ 0.05) in ACP GS, with statistically significant differences compared to Cit-ACP GS and flat surfaces (p value $\leq$ 0.0001). These results confirmed the activation and preservation of ALP protein and osteogenic commitment by Ad-MSCs seeded on ACP GS, as ALP is a reliable marker for osteogenic differentiation produced by osteogenic cells such as osteoblasts [73,74].

Therefore, the well-oriented and thicker nano-needles of ACP GS may have a strong mechanical impact on cells, influencing the induction and timing of the osteogenic differentiation process. Indeed, there is increasing recognition of the role played by the symmetry, regularity, and periodicity of nano-topographical patterns in upregulating the expression of osteogenic markers during MSC differentiation [75-77]. The evaluation of the osteogenic potential by ANSs in the proposed experimental plan represents a preliminary investigation to determine if these surfaces can trigger the early-stage regeneration process of bone tissue. Further evaluation through a longer-term experimental plan, focusing on the expression and function of proteins and genes involved in the late-stage osteogenic pathway, will be necessary to draw more solid conclusions and understand how different ANS properties can affect the entire osteogenic process.

In conclusion, both ANSs exhibited very high cytocompatibility with human cells, demonstrating promising results in terms of cell viability, proliferation, and morphology compared to flat surfaces. Specifically, ACP GS significantly promotes cell adhesion and triggers the commitment of Ad-MSCs to the osteogenic lineage, making it potentially suitable as antibacterial surface which regenerative potential for bone tissue. While nanostructured surfaces elicit stronger responses from cells compared to flat surfaces, the morphology, organization, and size of ANS nano-needles has different impacts on diverse cell populations. The thinner and less ordered Cit-ACP GS exhibited the strongest antibacterial action as well as the highest proliferation of VERO epithelial cells, while the well-aligned and thicker nano-needles of ACP GS demonstrate to stimulate more Ad-MSCs activity.

4. Conclusions

In this work we have produced oriented nano-needle structures of CaP using a straightforward bottom-up biomimetic approach. Employing ACP and Cit-ACP as substrates enabled the growth of ANSs with distinct topographic characteristics, including needle height, diameter, tip diameter, inter-needle distance, crystallinity, and crystal structure. Our analyses revealed that the ANSs exhibited a robust bactericidal effect against both antibiotic-resistant Gram-negative and Gram-positive bacterial strains even at short contact times, effectively eliminating up to 75 % of the bacterial population. The bactericidal activity demonstrated a correlation with nanostructure features, particularly the effectiveness of thinner and less oriented nano-needles, leading to the simultaneous rupture of the bacterial membrane and induction of oxidative stress in Gram-negative bacterial strains. Furthermore, we proved that the CaP-based ANS were highly biocompatible for mammalian epithelial cells and human mesenchymal stem cells, stimulating their proliferation and colonization onto the nanostructured surfaces. Also, the cytocompatibility of MSCs was correlated to the nano-topography of ANSs where thicker and well-aligned nano-needles stimulated more proliferation, adhesion, and accelerates differentiation timing of stem cells. These findings emphasize the influential role that ANSs features can play in cellular responses, offering insights into potential strategies for developing customized biomaterials with enhanced biocompatibility. This work advances the fundamental understanding of the contact-based bactericidal mechanisms of ANSs, elucidating the influence of ANSs nanostructure on both bacterial and mammal cells. Moreover, these results provide an encouraging premise for the development of materials with ANS-functionalized surfaces that could exhibit simultaneously antibacterial, bioactive, and cell instructive towards regeneration. In particular, the generation of CaP-based ANSs could be a promising approach for the treatment of antibiotic-resistant infections in orthopedics and implantology.

Declaration of competing interest

The authors declare that they have no known competing financial interests or personal relationships that could have appeared to influence the work reported in this paper.

CRediT authorship contribution statement

Lorenzo Degli Esposti: Writing – review & editing, Writing – original draft, Visualization, Resources, Investigation, Formal analysis, Conceptualization. **Damiano Squitieri:** Writing – review & editing, Writing – original draft, Visualization, Resources, Investigation, Formal analysis. **Camilla Fusacchia:** Writing – review & editing, Writing – original draft, Visualization, Resources, Investigation, Formal analysis. **Giada Bassi:** Writing – review & editing, Writing – original draft, Resources, Investigation, Formal analysis. **Riccardo Torelli:** Writing – review & editing, Methodology, Formal analysis. **Davide Altamura:** Writing – review & editing, Investigation, Formal analysis. **Erika Manicone:** Formal analysis, Data curation. **Silvia Panseri:** Writing – review & editing, Supervision, Methodology. **Alessio Adamiano:** Writing – review & editing, Investigation, Formal analysis. **Cinzia Giannini:** Writing – review & editing, Formal analysis. **Monica Montesi:** Writing – review & editing, Supervision, Methodology. **Francesca Bugli:** Writing – review & editing, Writing – original draft, Supervision, Methodology, Funding acquisition, Conceptualization. **Michele Iafisco:** Writing – review & editing, Writing – original draft, Supervision, Methodology, Funding acquisition, Conceptualization.

Acknowledgments

We acknowledge the Italian Ministry of University and Research (MUR) (Project “CHANCE” PRIN 2022, Research Grant 2022CCN7WM, founded by the European Union—NextGenerationEU) for providing financial support to this work. This work was also partially supported by the research project “Potentiating the Italian Capacity for Structural Biology Services in Instruct Eric” (Acronym: ITACA.SB, project n° IR0000009) within the call MUR D.D. 0003264 dated 28/12/2021 PNRR M4/C2/L3.1.1, funded by the European Union-NextGenerationEU.

Supplementary materials

Supplementary material associated with this article can be found, in the online version, at doi:10.1016/j.actbio.2024.08.001.

References

[1] L.J. Shallcross, S.J. Howard, T. Fowler, S.C. Davies, Tackling the threat of antimicrobial resistance: from policy to sustainable action, Philos. Trans. R. Soc. B 370 (1670) (2015) 20140082.
[2] M.S. Mulani, E.E. Kamble, S.N. Kumkar, M.S. Tawre, K.R. Pardesi, Emerging strategies to combat ESKAPE pathogens in the era of antimicrobial resistance: a review, Front. Microbiol. 10 (2019) 539.
[3] A. Tripathy, P. Sen, B. Su, W.H. Briscoe, Natural and bioinspired nanostructured bactericidal surfaces, Adv. Colloid Interface Sci 248 (2017) 85–104.
[4] E.P. Ivanova, J. Hasan, H.K. Webb, V.K. Truong, G.S. Watson, J.A. Watson, V.A. Baulin, S. Pogodin, J.Y. Wang, M.J. Tobin, Natural bactericidal surfaces: mechanical rupture of *Pseudomonas aeruginosa* cells by cicada wings, Small. 8 (16) (2012) 2489–2494.
[5] S. Pogodin, J. Hasan, V.A. Baulin, H.K. Webb, V.K. Truong, V. Boshkovikj, C.J. Fluke, G.S. Watson, J.A. Watson, R.J. Crawford, Biophysical model of bacterial cell interactions with nanopatterned cicada wing surfaces, Biophys. J. 104 (4) (2013) 835–840.

[6] J.M.A. Blair, M.A. Webber, A.J. Baylay, D.O. Ogbolu, L.J.V. Piddock, Molecular mechanisms of antibiotic resistance, Nat. Rev. Microbiol. 13 (1) (2015) 42–51.
[7] V.T. Pham, V.K. Truong, A. Orlowska, S. Ghanaati, M. Barbeck, P. Booms, A.J. Fulcher, C.M. Bhadra, R. Buividas, V. Baulin, Race for the surface": eukaryotic cells can win, ACS Appl. Mater. Interfaces 8 (34) (2016) 22025–22031.
[8] K. Modaresifar, S. Azizian, M. Ganjian, L.E. Fratila-Apachitei, A.A. Zadpoor, Bactericidal effects of nanopatterns: a systematic review, Acta Biomater. 83 (2019) 29–36.
[9] S.G. Higgins, M. Becce, A. Belessiotis-Richards, H. Seong, J.E. Sero, M.M. Stevens, High-aspect-ratio nanostructured surfaces as biological metamaterials, Adv. Mater. 32 (9) (2020) 1903862.
[10] J. Gómez-Morales, M. Iafisco, J.M. Delgado-López, S. Sarda, C. Drouet, Progress on the preparation of nanocrystalline apatites and surface characterization: overview of fundamental and applied aspects, Prog. Cryst. Growth Charact. Mater. 59 (1) (2013) 1–46.
[11] W. Ahmed, Z. Zhai, C. Gao, Adaptive antibacterial biomaterial surfaces and their applications, Mater. Today Bio 2 (2019) 100017.
[12] B. Spellberg, B.A. Lipsky, Systemic antibiotic therapy for chronic osteomyelitis in adults, Clin. Infect. Dis. 54 (3) (2012) 393–407.
[13] D.P. Linklater, V.A. Baulin, S. Juodkazis, R.J. Crawford, P. Stoodley, E.P. Ivanova, Mechano-bactericidal actions of nanostructured surfaces, Nat. Rev. Microbiol. 19 (1) (2021) 8–22.
[14] A.-W. Xu, Y. Ma, H. Cölfen, Biomimetic mineralization, J. Mater. Chem. 17 (5) (2007) 415–449.
[15] F. Carella, L. Degli Esposti, D. Barreca, G.A. Rizzi, G. Martra, P. Ivanchenko, G.E. Casado, J.G. Morales, J.M.D. Lòpez, A. Tampieri, Role of citrate in the formation of enamel-like calcium phosphate oriented nanorod arrays, CrystEngComm. 21 (32) (2019) 4684–4689.
[16] K. Onuma, M. Iijima, Artificial enamel induced by phase transformation of amorphous nanoparticles, Sci. Rep. 7 (1) (2017) 2711.
[17] M. Iijima, K. Onuma, Roles of fluoride on octacalcium phosphate and apatite formation on amorphous calcium phosphate substrate, Cryst. Growth Des. 18 (4) (2018) 2279–2288.
[18] M. Iglesias-Fernandez, J. Buxadera-Palomero, J.-M. Sadowska, M. Espanol, M.-P. Ginebra, Implementation of bactericidal topographies on biomimetic calcium phosphates and the potential effect of its reactivity, Biomater. Adv. 136 (2022) 212797.
[19] X. Ge, J. Zhao, K.D. Esmeryan, X. Lu, Z. Li, K. Wang, F. Ren, Q. Wang, M. Wang, B. Qian, Cicada-inspired fluoridated hydroxyapatite nanostructured surfaces synthesized by electrochemical additive manufacturing, Mater. Des. 193 (2020) 108790.
[20] G. Bhardwaj, H. Yazici, T.J. Webster, Reducing bacteria and macrophage density on nanophase hydroxyapatite coated onto titanium surfaces without releasing pharmaceutical agents, Nanoscale 7 (18) (2015) 8416–8427.
[21] H.-T. Liao, C.-T. Chen, Osteogenic potential: comparison between bone marrow and adipose-derived mesenchymal stem cells, World J. Stem Cells 6 (3) (2014) 288.
[22] N. Shabestani, H. Mousazadeh, F. Shayegh, S. Gholami, A. Mota, N. Zarghami, Osteogenic differentiation of adipose-derived stem cells on dihydroartemisinin electrospun nanofibers, J. Biol. Eng. 16 (1) (2022) 15.
[23] M. Iafisco, L. Degli Esposti, G.B. Ramírez-Rodríguez, F. Carella, J. Gómez–Morales, A.C. Ionescu, E. Brambilla, A. Tampieri, J.M. Delgado-López, Fluoride–doped amorphous calcium phosphate nanoparticles as a promising biomimetic material for dental remineralization, Sci. Rep. 8 (1) (2018) 17016.
[24] M.D. Abràmoff, P.J. Magalhães, S.J. Ram, Image processing with ImageJ, Biophoton. Int. 11 (7) (2004) 36–42.
[25] D. Altamura, R. Lassandro, F. Vittoria, L. De Caro, D. Siliqi, M. Ladisa, C. Giannini, X-ray microimaging laboratory (XMI-LAB), J. Appl. Crystallogr. 45 (4) (2012) 869–873.
[26] D. Siliqi, L. De Caro, M. Ladisa, F. Scattarella, A. Mazzone, D. Altamura, T. Sibillano, C. Giannini, SUNBIM: a package for X-ray imaging of nano-and biomaterials using SAXS, WAXS, GISAXS and GIWAXS techniques, J. Appl. Crystallogr. 49 (3) (2016) 1107–1114.
[27] J. Rodríguez-Carvajal, Recent advances in magnetic structure determination by neutron powder diffraction, Physica B 192 (1–2) (1993) 55–69.
[28] J.L. Lábár, Consistent indexing of a (set of) single crystal SAED pattern with the ProcessDiffraction program, Ultramicroscopy. 103(3) (2005) 237–249.
[29] S. Krukowski, M. Karasiewicz, W. Kolodziejski, Convenient UV-spectrophotometric determination of citrates in aqueous solutions with applications in the pharmaceutical analysis of oral electrolyte formulations, J. Food Drug Anal. 25 (3) (2017) 717–722.
[30] J. Schindelin, I. Arganda-Carreras, E. Frise, V. Kaynig, M. Longair, T. Pietzsch, S. Preibisch, C. Rueden, S. Saalfeld, B. Schmid, Fiji: an open-source platform for biological-image analysis, Nat. Methods 9 (7) (2012) 676–682.
[31] K.J. Livak, T.D. Schmittgen, Analysis of relative gene expression data using real-time quantitative PCR and the 2− ΔΔCT method, Methods 25 (4) (2001) 402–408.
[32] C. Teixeira, M. Hatori, P. Leboy, M. Pacifici, I. Shapiro, A rapid and ultrasensitive method for measurement of DNA, calcium and protein content, and alkaline phosphatase activity of chondrocyte cultures, Calcif. Tissue Int. 56 (1995) 252–256.
[33] S.K. Akdere, Z.U. Aydin, D. Erdönmez, Antimicrobial effectiveness of different irrigation activation techniques on teeth with artificial internal root resorption and contaminated with Enterococcus faecalis: a confocal laser scanning, icroscopy analysis, Lasers. Med. Sci. 38 (1) (2023) 89.
[34] L.M. Rodríguez-Lorenzo, J.N. Hart, K.A. Gross, Structural and chemical analysis of well-crystallized hydroxyfluorapatites, J. Phys. Chem. B 107 (33) (2003) 8316–8320.
[35] J.M. Hughes, M. Cameron, K.D. Crowley, Structural variations in natural F, OH, and Cl apatites, Am. Mineral. 74 (7–8) (1989) 870–876.
[36] Q. Cui, T. Liu, X. Li, K. Song, D. Ge, Nanopillared polycarbonate surfaces having variable feature parameters as bactericidal coatings, ACS Appl. Nano Mater. 3 (5) (2020) 4599–4609.
[37] L. Degli Esposti, A. Adamiano, A. Tampieri, G.B. Ramirez-Rodriguez, D. Siliqi, C. Giannini, P. Ivanchenko, G. Martra, F.-H. Lin, J.M. Delgado-López, Combined effect of citrate and fluoride ions on hydroxyapatite nanoparticles, Cryst. Growth Des 20 (5) (2020) 3163–3172.
[38] H. Straub, L. Eberl, M. Zinn, R.M. Rossi, K. Maniura-Weber, Q. Ren, A microfluidic platform for in situ investigation of biofilm formation and its treatment under controlled conditions, J. Nanobiotechnol. 18 (2020) 1–12.
[39] T. Duanis-Assaf, M. Reches, Factors influencing initial bacterial adhesion to antifouling surfaces studied by single-cell force spectroscopy, iScience 27 (2) (2024).
[40] C.H. Liao, L. Shollenberger, Survivability and long-term preservation of bacteria in water and in phosphate-buffered saline, Lett. Appl. Microbiol. 37 (1) (2003) 45–50.
[41] J. Hasan, H.K. Webb, V.K. Truong, S. Pogodin, V.A. Baulin, G.S. Watson, J.A. Watson, R.J. Crawford, E.P. Ivanova, Selective bactericidal activity of nanopatterned superhydrophobic cicada Psaltoda claripennis wing surfaces, Appl. Microbiol. Biotechnol. 97 (2013) 9257–9262.
[42] S. Wu, F. Zuber, K. Maniura-Weber, J. Brugger, Q. Ren, Nanostructured surface topographies have an effect on bactericidal activity, J. Nanobiotechnol. 16 (2018) 1–9.
[43] F. Viela, I. Navarro-Baena, J.J. Hernández, M.R. Osorio, I. Rodríguez, Moth–eye mimetic cytocompatible bactericidal nanotopography: a convergent design, Bioinspir. Biomim. 13 (2) (2018) 026011.
[44] E.P. Ivanova, J. Hasan, H.K. Webb, G. Gervinskas, S. Juodkazis, V.K. Truong, A.H. Wu, R.N. Lamb, V.A. Baulin, G.S. Watson, Bactericidal activity of black silicon, Nat. Commun. 4 (1) (2013) 2838.
[45] J. Jenkins, J. Mantell, C. Neal, A. Gholinia, P. Verkade, A.H. Nobbs, B. Su, Antibacterial effects of nanopillar surfaces are mediated by cell impedance, penetration and induction of oxidative stress, Nat. Commun. 11 (1) (2020) 1626.
[46] V.M. Wu, S. Tang, V. Uskokovic, Calcium phosphate nanoparticles as intrinsic inorganic antimicrobials: the antibacterial effect, ACS Appl. Mater. Interfaces 10 (40) (2018) 34013–34028.
[47] M. Firouzi, Z. Haghighijoo, M. Eskandari, M. Mohabbati, R. Miri, M.H. Jamei, A. Poustforoosh, S. Nazari, O. Firuzi, M. Khoshneviszadeh, N. Edraki, Synthesis and cytotoxic activity evaluation of novel imidazopyridine carbohydrazide derivatives, BMC Chem. 18 (1) (2024) 6.
[48] Z. Jahed, S. Molladavoodi, B.B. Seo, M. Gorbet, T.Y. Tsui, M.R. Mofrad, Cell responses to metallic nanostructure arrays with complex geometries, Biomaterials 35 (34) (2014) 9363–9371.
[49] K. Anselme, P. Davidson, A. Popa, M. Giazzon, M. Liley, L. Ploux, The interaction of cells and bacteria with surfaces structured at the nanometre scale, Acta Biomater. 6 (10) (2010) 3824–3846.
[50] J. Albuschies, V. Vogel, The role of filopodia in the recognition of nanotopographies, Sci. Rep. 3 (1) (2013) 1–9.
[51] B.T. Estes, B.O. Diekman, J.M. Gimble, F. Guilak, Isolation of adipose-derived stem cells and their induction to a chondrogenic phenotype, Nat. Protoc. 5 (7) (2010) 1294–1311.
[52] E. Martinez, E. Engel, J. Planell, J. Samitier, Effects of artificial micro-and nano-structured surfaces on cell behaviour, Ann. Anat. 191 (1) (2009) 126–135.
[53] J. Wei, S. Heo, D. Kim, S. Kim, Y. Hyun, J.-W. Shin, Comparison of physical, chemical and cellular responses to nano-and micro-sized calcium silicate/poly (ϵ-caprolactone) bioactive composites, J. R. Soc. Interface 5 (23) (2008) 617–630.
[54] C.E. Turner, Paxillin and focal adhesion signalling, Nat. Cell Biol. 2 (12) (2000) E231–E236.
[55] D.D. Schlaepfer, C.R. Hauck, D.J. Sieg, Signaling through focal adhesion kinase, Prog. Biophys. Mol. Biol. 71 (3–4) (1999) 435–478.
[56] M. Wozniak, A. Fausto, C.P. Carron, D.M. Meyer, K.A. Hruska, Mechanically strained cells of the osteoblast lineage organize their extracellular matrix through unique sites of $\alpha v\beta 3$-integrin expression, J. Bone Miner. Res. 15 (9) (2000) 1731–1745.
[57] M.D. Schaller, Paxillin: a focal adhesion-associated adaptor protein, Oncogene 20 (44) (2001) 6459–6472.
[58] D. Riveline, E. Zamir, N.Q. Balaban, U.S. Schwarz, T. Ishizaki, S. Narumiya, Z. Kam, B. Geiger, A.D. Bershadsky, Focal contacts as mechanosensors: externally applied local mechanical force induces growth of focal contacts by an mDia1-dependent and ROCK-independent mechanism, J. Cell Biol. 153 (6) (2001) 1175–1186.
[59] N.J. Sniadecki, C.S. Chen, Microfabricated silicone elastomeric post arrays for measuring traction forces of adherent cells, Methods Cell Biol. 83 (2007) 313–328.
[60] M. Ripamonti, B. Wehrle-Haller, I. de Curtis, Paxillin: a hub for mechano-transduction from the $\beta 3$ integrin-talin-kindlin axis, Front. Cell Dev. Biol. 10 (2022) 852016.
[61] Y. Sawada, M.P. Sheetz, Force transduction by Triton cytoskeletons, J. Cell Biol. 156 (4) (2002) 609–615.
[62] J. Petzold, E. Gentleman, Intrinsic mechanical cues and their impact on stem cells and embryogenesis, Front. Cell Dev. Biol. 9 (2021) 761871.

[63] A.S. Vasilevich, S. Vermeulen, M. Kamphuis, N. Roumans, S. Eroumé, D.G. Hebels, J. van de Peppel, R. Reihs, N.R. Beijer, A. Carlier, On the correlation between material-induced cell shape and phenotypical response of human mesenchymal stem cells, Sci. Rep. 10 (1) (2020) 18988.
[64] J. Fiedler, B. Özdemir, J. Bartholomä, A. Plettl, R.E. Brenner, P. Ziemann, The effect of substrate surface nanotopography on the behavior of multipotnent mesenchymal stromal cells and osteoblasts, Biomaterials 34 (35) (2013) 8851–8859.
[65] D.D. Deligianni, N.D. Katsala, P.G. Koutsoukos, Y.F. Missirlis, Effect of surface roughness of hydroxyapatite on human bone marrow cell adhesion, proliferation, differentiation and detachment strength, Biomaterials 22 (1) (2000) 87–96.
[66] W.-K. Lee, S.-M. Lee, H.-M. Kim, Effect of surface morphology of calcium phosphate on osteoblast-like HOS cell responses, J. Ind. Eng. Chem. 15 (5) (2009) 677–682.
[67] S. Samavedi, A.R. Whittington, A.S. Goldstein, Calcium phosphate ceramics in bone tissue engineering: a review of properties and their influence on cell behavior, Acta Biomater. 9 (9) (2013) 8037–8045.
[68] R.T. Franceschi, C. Ge, G. Xiao, H. Roca, D. Jiang, Transcriptional regulation of osteoblasts, Cells Tissues. Organs 189 (1–4) (2008) 144–152.
[69] C.A. Gersbach, B.A. Byers, G.K. Pavlath, A.J. García, Runx2/Cbfa1 stimulates transdifferentiation of primary skeletal myoblasts into a mineralizing osteoblastic phenotype, Exp. Cell Res. 300 (2) (2004) 406–417.
[70] L. Malaval, F. Liu, P. Roche, J.E. Aubin, Kinetics of osteoprogenitor proliferation and osteoblast differentiation in vitro, J. Cell. Biochem. 74 (4) (1999) 616–627.
[71] J. Jeong, J.H. Kim, J.H. Shim, N.S. Hwang, C.Y. Heo, Bioactive calcium phosphate materials and applications in bone regeneration, Biomater. Res. 23 (1) (2019) 1–11.
[72] S.H.Z. Ariffin, K.W. Lim, R.M.A. Wahab, Z.Z. Ariffin, R.D.R. Din, M.A. Shahidan, A.N. Johari, I.Z.Z. Abidin, Gene expression profiles for in vitro human stem cell differentiation into osteoblasts and osteoclasts: a systematic review, PeerJ. 10 (2022) e14174.
[73] B. Reible, G. Schmidmaier, M. Prokscha, A. Moghaddam, F. Westhauser, Continuous stimulation with differentiation factors is necessary to enhance osteogenic differentiation of human mesenchymal stem cells in-vitro, Growth Factors 35 (4–5) (2017) 179–188.
[74] B. Reible, G. Schmidmaier, A. Moghaddam, F. Westhauser, Insulin-like growth factor-1 as a possible alternative to bone morphogenetic protein-7 to induce osteogenic differentiation of human mesenchymal stem cells in vitro, Int. J. Mol. Sci. 19 (6) (2018) 1674.
[75] W. Chen, Y. Shao, X. Li, G. Zhao, J. Fu, Nanotopographical surfaces for stem cell fate control: engineering mechanobiology from the bottom, Nano Today 9 (6) (2014) 759–784.
[76] A. Barlian, K. Vanya, Nanotopography in directing osteogenic differentiation of mesenchymal stem cells: potency and future perspective, Future Sci. OA 8 (1) (2022) FSO765.
[77] M.-J. Kim, B. Lee, K. Yang, J. Park, S. Jeon, S.H. Um, D.-I. Kim, S.G. Im, S.-W. Cho, BMP-2 peptide-functionalized nanopatterned substrates for enhanced osteogenic differentiation of human mesenchymal stem cells, Biomaterials 34 (30) (2013) 7236–7246.